TFE3 fusion proteins drive oxidative metabolism, ferroptosis resistance and general RNA synthesis in translocation renal cell carcinoma

Alexandra Helleux[1,2,3,4], Guillaume Davidson[1,2,3,4], Antonin Lallement[1,2,3,4], Alexandre Haller[1,2,3,4], Isabelle Michel[1,2,3,4], Anas Fadloun[1,2,3,4], Christelle Thibault-Carpentier[1,2,3,4], Xiaoping Su[5], Véronique Lindner[6], Thibaut Tricard[7], Hervé Lang[7], Nizar Tannir[8], Irwin Davidson[1,2,3,4,10] and Gabriel G. Malouf[1,2,3,4,9,10]

1. Institut de Génétique et de Biologie Moléculaire et Cellulaire, BP 163, 67404 Illkirch, France

2. Centre National de la Recherche Scientifique, UMR7104, 67404 Illkirch, France

3. Institut National de la Santé et de la Recherche Médicale, U1258, 67404 Illkirch, France

4. Université de Strasbourg, 67404 Illkirch, France

5. Department of Bioinformatics and Computational Biology, The University of Texas MD Anderson Cancer Center, Houston, Texas, USA

6. Department of Pathology, Strasbourg University Hospital, Strasbourg, France

7. Department of Urology, Strasbourg University Hospital, Strasbourg, France

8. Department of Genitourinary Medical Oncology, The University of Texas MD Anderson Cancer Center Houston, Texas, USA

9. Department of Medical Oncology, Institut de Cancérologie de Strasbourg-Europe, Strasbourg, France

10. These authors should be considered equally as co-senior authors.

Keywords: translocation renal cell carcinoma, TFE3, Metabolism, Ferroptosis, RNA synthesis, cancer associated fibroblasts

Conflict of interest statement: G.M. reported grant from INCA, Fondation ARC and MSD AVENIR. I.D. reported grant from la Ligue Contre le Cancer.

Abstract

The oncogenic mechanisms by which TFE3 fusion proteins drive translocation renal cell carcinoma (tRCC) are poorly characterised. Here, we integrated loss and gain of function experiments with multi-omics analyses in tRCC cell lines and patient tumors. High nuclear accumulation of NONO-TFE3 or PRCC-TFE3 fusion proteins promotes their broad binding across the genome at H3K27ac-marked active chromatin, engaging a core set of M/E-box-containing regulatory elements to activate specific gene expression programs as well as promiscuous binding to active promoters to stimulate mRNA synthesis. Within the core program, TFE3 fusions directly regulate genes involved in ferroptosis resistance and oxidative phosphorylation metabolism (OxPhos) increasing functional OxPhos levels. Consequently, human tRCC tumors display high OxPhos scores that persist during their epithelial to mesenchymal transition (EMT). We further show that tRCC tumour aggressiveness is related to their EMT which although enriched in tumours harbouring ASPSCR1-TFE3 fusions, is also a frequent feature of tumours harbouring other TFE3 fusions. In tRCC tumours, the presence of mesenchymal tRCC cancer cells associates with that of myofibroblast cancer-associated fibroblasts (myCAFs) that are both hallmarks of poor prognostic outcomes. We define tRCC as a novel metabolic subtype of renal cancer and provide unique insights into how broad genomic binding of TFE3 fusion proteins regulates OxPhos and ferroptosis resistance and more generally stimulates RNA synthesis.

Significance.

This study advances understanding of the molecular mechanisms underlying oncogenic transformation by TFE3 fusion proteins in translocation renal cell carcinoma and defines features of tumour cells and their microenvironment that negatively impact patient outcome.

Integrative multi-omics analyses reveal how extensive genomic binding of TFE3 fusion proteins drives oncogenic programs and identify novel potential therapeutic targets.

Introduction

TFE3 and TFEB are members of the Microphthalmia-associated Transcription (MiT) family that regulate lysosomal function, nutrient/stress response and drug resistance [1]. Translocation renal cell carcinomas (tRCC) are characterised by genetic translocation events involving one member of the (MiT) family, most frequently *TFE3* (90% of cases) [2,3]. TRCC is a rare subtype of kidney cancer that represents 1-4% of all adults RCC[4,5], but is the most frequent RCC arising in children and adolescents [1,6,7]. The translocations result in expression of chimeric fusion proteins comprising TFE3 and another gene partner, under the control of constitutively active gene promoters[8]. The complexity of tRCC is underscored by the identification of over 20 TFE3-partners, accentuating histological and clinical heterogeneity. Among these, *SFPQ*, *ASPSCR1*, *PRCC*, and *NONO* are the most frequent fusion partners. Aside these translocations, no other highly recurrent mutations have been identified, suggesting that the fusion proteins are the primary drivers of transformation. In agreement with this, all fusion proteins retain the TFE3 DNA binding and dimerization (basic-helix-loop-helix leucine-zipper; bHLH-LZ) domains allowing them to bind to cis-regulatory elements in the genome. Despite recent recognition of tRCC as a distinct RCC subtype, the precise oncogenic mechanisms fueling tRCC tumorigenesis remain elusive. Consequently, there is an urgent medical need to unravel the molecular function of TFE3-fusion proteins to comprehensively understand the molecular basis of tRCC and identify novel therapeutic targets.

To better understand how TFE3 fusion proteins drive transformation in tRCC, we performed gain and loss of function experiments complemented by multi-omics approaches to profile genome occupancy of TFE3 fusions, identify active cis-regulatory elements and characterize the gene expression programs under their control in model cell lines and human tumours. Our findings revealed that NONO-TFE3 and PRCC-TFE3 fusions exhibit broad binding to thousands of sites across the genome, engaging distal and proximal M/E-box-

containing regulatory elements, as well as promiscuously associating with active promoters. Amongst the core regulated genes are those driving oxidative phosphorylation (OxPhos) metabolism, culminating in elevated OxPhos levels in tRCC cells, and those promoting ferroptosis resistance. Analyses of RNA-seq of tRCC patient tumors demonstrated heightened OxPhos scores confirming the observations from the cell lines. Remarkably, elevated OxPhos score persisted in tumors that had undergone epithelial to mesenchymal transition (EMT), a known marker of tumor aggressiveness. Furthermore, using transcriptional signatures derived from clear cell renal carcinoma (ccRCC), we revealed that tRCC tumors with EMT signatures were enriched in myofibroblastic cancer-associated fibroblasts (myCAFs) whose presence correlated with poorer survival. Thus, EMT and presence of myCAFs emerge as common hallmarks, adversely impacting the prognosis for both ccRCC and tRCC.

Results

Abundant constitutive nuclear expression of TFE3 fusion proteins is essential for tRCC cell line viability

To address the role of TFE3 fusion proteins in tRCC, we used 4 cell lines expressing either NONO-TFE3 (lines UOK109, TF1) or PRCC-TFE3 (UOK120, UOK146). Each fusion protein presents a different breakpoint within TFE3, but conserve its bHLH-LZ domain maintaining their ability to specifically bind DNA. To assess expression of TFE3 fusion proteins compared to native TFE3, we performed immunoblots on extracts from the above lines as well as 2 non-transformed renal cell lines (RPTEC, HEK293T), 4 clear-cell (cc)RCC lines (RCC4, UOK121, A-498, 786-O) and 2 papillary (p)RCC lines (UOK112, ACHN). High expression of NONO-TFE3 and lower expression of PRCC-TFE3 fusions in the corresponding tRCC lines was observed, while expression of native TFE3 in the other cell lines was variable, but considerably lower than the fusion proteins **(Fig. S1A)**. In contrast, no native TFE3 protein

was visible in tRCC lines consistent with the *TFE3* gene location on the X chromosome and hence in cells of male origin, UOK109, TF1 and UOK120, the single copy of *TFE3* is subject to translocation[9–11] whereas in the female UOK146 line expression of the non-translocated allele transcript is silenced[10]. In addition, biochemical fractionation of the nuclear and cytoplasmic compartments showed strong enrichment of TFE3 fusion proteins in the nucleus similar to what is observed with the control BRG1, the catalytic subunit of the SWI/SNF chromatin remodelling complex **(Fig. S1B)**. Thus, the tRCC cell lines abundantly express the expected nuclear TFE3-fusion proteins.

To characterize the gene expression programs of the tRCC cell lines, triplicate RNA-seq was performed for each line. More than 80% of the 3000 most highly expressed protein-coding genes were common to all 4 cell lines **(Fig. S1C)** and were enriched for pathways previously associated with function of native TFE3 such as lysosome function and endocytosis (**Fig. S1D**). In addition, various metabolic pathways were enriched notably those linked to the electron transport chain, oxidative phosphorylation (OxPhos), reactive oxygen species (ROS) and carbon metabolism **(Fig. S1D)**. Each line displayed hybrid EMT-type markers **(Fig. S1E)**. For example, while TF1 and UOK146 showed highest expression of the epithelial marker *EPCAM*, they overexpress the mesenchymal *PRXX1* and *SNAI1/2* genes, respectively. Of note, the EMT regulators *SNAI1/2* were mostly expressed in the PRRC-TFE3 lines as compared to *TWIST1* or *TWIST2* most expressed in the NONO-TFE3 lines. Overall, UOK120 appeared to be the most mesenchymal line with the lowest expression of most epithelial markers, and higher expression of multiple mesenchymal markers and/or regulators **(Fig. S1E)**.

To assess the role of TFE3 fusion proteins in the transformed phenotype, their expression was silenced using siRNA specifically directed against the TFE3 C-terminal region and compared with non-targeting control siRNA. RT-qPCR indicated efficient knockdown of TFE3 in the 2 PRCC-TFE3 lines (UOK120, UOK146; >80% reduction) as compared to control.

Less efficient silencing was observed in the NONO-TFE3 lines (UOK109, TF1) perhaps due to the higher fusion expression. (**Fig. 1A**). Similar effects were seen on immunoblots with strongly reduced levels of fusion protein in UOK120 and UOK146 lines, with less attenuated effects in UOK109 and TF1 lines **(Fig. 1B)**. TFE3 fusion silencing dramatically reduced colony forming ability with a reduction reaching 90% for both NONO-TFE3 cell lines as compared to 60% and 80% for UOK120 and UOK146 lines, respectively **(Fig. 1C)**. Thus, high levels of fusion protein were essential for tRCC cell viability irrespective of their epithelial/mesenchymal states.

TFE3 fusions drive expression of genes involved in OxPhos

To identify genes regulated by TFE3 fusions, RNA-seq was performed on each cell line after siRNA-control (siCTR) or siRNA-TFE3 (siTFE3). Following silencing, the number of reads at the fusion junction and read coverage over TFE3 exons present in both NONO- and PRCC-TFE3 fusions were strongly decreased **(Figs. S2A-B)**. Following TFE3-fusion protein silencing, we observed up- or down-regulation of hundreds of genes (range: ~200-500) in each tRCC cell line using a standard cut-off (log2 fold change > +/- 1, and adjusted p-value <0.05, **Fig. S2B and Dataset S1**).

Gene Set Enrichment Analyses (GSEA) using the Hallmarks gene sets showed consistent down-regulation of the Oxidative Phosphorylation (OxPhos) pathway in all tRCC lines. In addition, we observed enrichment for down-regulation of oncogenic pathways in several cell lines such as MYC targets and pathways related to cell cycle and proliferation (E2F targets, G2M checkpoint; **Figs. 1D and S2C)**. Limited pathways were enriched in the up-regulated genes (**Fig. 1D**). Among the 200 genes comprising the GSEA OxPhos signature (**Dataset S2**), between 115 and 139 were down-regulated depending on the line, with 54 commonly down-regulated in all 4 lines (**Fig. 1E).** These genes encode multiple subunits of the mitochondrial respiration chain complexes I (*NDUF* (NADH:ubiquinone oxidoreductase), II (*SDHA/B*), III *UQC* (ubiquitol-cytochrome c oxidoreductase) and IV (*COX* cytochrome c-

oxidase) (**Fig. 1F**). In addition, multiple subunits of the V-type proton ATPase, a complex responsible for acidification of intracellular organelles notably lysosomes, also comprised in the GSEA OxPhos pathway, were down-regulated by siTFE3. These observations suggested a direct role of TFE3 fusions in regulating expression of genes involved in OxPhos metabolism.

To evaluate whether these gene expression changes affected OxPhos, mitochondrial activity was measured by profiling the Oxygen Consumption Rate (OCR) using the Agilent SeaHorse (**Fig. 1G**). Comparison of OCR activity showed higher basal and maximum respiration capacities in 3 of the tRCC lines compared to the 786-O and UOK121 ccRCC lines, the exception being TF1 (**Fig. 1H**).

To determine the contribution of the TFE3 fusions to the elevated OxPhos capacity, SeaHorse experiments were performed in siTFE3 versus siCTR cells 72h after transfection. Although basal OCR levels were unaffected, both maximum respiration and reserve capacity were significantly decreased after siTFE3 in UOK109, UOK146 and UOK120, with a tendency observed for TF1 line (**Fig. 1I**). These data showed that TFE3-fusions drive expression of genes involved in OxPhos resulting in a higher contribution of OxPhos to the metabolism of tRCC compared to ccRCC cell lines.

Ectopic expression of TFE3 fusions leads to loss of renal identity and stimulates OxPhos.

To determine whether TFE3 fusions can directly activate OxPhos, we performed gain of function experiments using HEK293T embryonic kidney cells. HEK293T cells were infected with lentiviral particles containing a Doxycycline (Dox)-inducible expression vector for either native TFE3 (T), NONO-TFE3 (NT), PRCC-TFE3 (PT) or GFP control. 24 hours after Dox addition, a strong induction was seen at both the mRNA (**Fig. 2A**) and protein expression levels with NONO-TFE3 accumulating to lower levels than PRCC-TFE3 (**Fig. 2B**). Under these

conditions, ectopic TFE3, NONO-TFE3 and PRCC-TFE3 proteins all accumulated in the nucleus (**Fig. 2C**).

To identify genes regulated by ectopic protein expression, we performed RNA-seq 24 hours after Dox induction. Ectopic TFE3 expression deregulated over 1000 genes as compared to the GFP control line using standard cut-off (log2FC>|1| and adj.p.val<0.05, **Fig. 2D and Dataset S3**). Most genes deregulated by native TFE3 expression were also deregulated using fusion proteins (**Figs. S3A-B)**, whereas additional gene sets either commonly or specifically deregulated by both fusion proteins were observed. Overall, 558 genes were up-regulated in all TFE3-expressing lines and linked to functions previously ascribed to native TFE3 such as lysosome, mTORC1-associated pathway or transport of small molecules through ion channels (**Fig. S3A**). Although fewer (71) common down-regulated genes were found, ontology showed they were linked to morphogenesis and development processes including kidney development suggesting that ectopic fusion protein expression may lead to loss of epithelial and kidney identity (**Fig. S3B)**.

While hallmark GSEA analysis showed few significant pathways for down-regulated genes, several pathways were enriched amongst up-regulated genes such mTORC1 signalling and immune signalling (TNFa signalling via NFkB, IFNg response; **Fig. 2E)**. Importantly and in line with loss of function experiments, OxPhos was up-regulated in all conditions (**Figs. 2E and S3C)**. Among the 200 genes in the OxPhos pathway, between 84 to 119 genes were up-regulated with 59 genes common to all 3 lines including those encoding subunits of complexes of the electron transport chain and the lysosomal V-ATPase, but also other genes involved in mitochondrial homeostasis and function (**Figs. 2F-G)**. In line with these observations, ectopic expression of TFE3, and to a greater extent TFE3 fusions enhanced basal and maximal OCR respiration as well as reserve capacity compared to the GFP control line (**Figs. 2H-I**). Thus,

both loss and gain of function converged to show that TFE3 fusion proteins activated genes of the OxPhos pathway leading to enhanced OxPhos metabolism.

TFE3 fusions bind promiscuously at active promoters and stimulate RNA synthesis

To better understand how the fusion proteins regulate gene expression, we performed Cut&Tag (C&T) in all 4 tRCC cell lines to profile TFE3 fusion protein binding along with H3K27ac ChIP-seq to identify active cis-regulatory elements. Read density analyses of the non-redundant TFE3 peaks from all lines revealed a large number of low occupied sites that did not coincide with H3K27ac (Cluster 14 in **Fig. S4A**). We therefore focussed our analyses on the 84 765 non-redundant sites strongly occupied in at least one of the 4 lines (**Fig. 3A)**. Using this set of highly occupied sites, we found that the number of TFE3 peaks was around 2-fold higher (65 000-78 000) in both NONO-TFE3 expressing lines compared to PRCC-TFE3 (33 000-42 000) lines, whereas comparable numbers (44 000-64 000) of H3K27ac ChIP-seq peaks were observed in each cell line (**Fig. S4B)**.

MEME-ChIP-analyses of the top 1000 TFE3 peaks in the UOK120 and UOK146 lines revealed strong enrichment in the M/E-box motif, that was the only enriched motif (**Fig. S4C**). In contrast, analogous analyses of the UOK109 and TF1 TFE3 peaks revealed enrichment of GC-rich SP1/KLF-type motifs in addition to the M/E-box motif. Analyses of motif locations showed the M/E-box motif protected at the peak centre, whereas the other motifs were spread across the peaks. Similar results were found using RSAT software, where the M/E-box motif was highly represented in the UOK120 and UOK146 peaks, but was lower ranked in the other lines, where in addition the GC-rich SP1/KLF and NFY motifs were also detected (**Fig. S4D**). Thus, the fusion proteins bind to their cognate M/E-box motif, but additional indirect binding was seen, in particular of NONO-TFE3.

The GC-rich SP1/KLF and NFY-binding CAAT-box motifs are prevalent in proximal promoters with the CATT-box located around 70 nucleotides upstream of the transcription start site (TSS) [12]. Read density analyses showed that many of the 84 765 non-redundant were associated with H3K27ac either in a common or cell-specific manner (**Fig. 3A**) and consistent with the presence of SP1 and CATT-motifs, strong TFE3 fusion occupancy of ≈8 700 active H3K27ac-marked promoters was seen (**Fig. 3B**). TFE3 fusion binding was also seen at 19 040 promoter distal regions (**Fig. 3C**) with a set of sites commonly occupied in all 4 lines (clusters 1-14), but showing differential association with H3K27ac (clusters 8-14). The remaining sites showed cell-specific occupancy such as cluster 15 preferentially occupied by NONO-TFE3 or clusters 16-19 corresponding to sites selectively occupied and/or marked by H3K27ac in a cell line-specific manner.

To consolidate these findings, we performed TFE3 C&T in the HEKT cells described above. As an additional control, these experiments were performed with an independent TFE3 antibody that was used in parallel in a replicate C&T in UOK109 cells. Comparison of the UOK109 data with the 2 TFE3 antibodies revealed high concordance of the strongly bound sites, with only the weak binding sites showing less signal with the second antibody (**Fig. S5**). In the HEK-GFP cells, binding of endogenous TFE3 was seen at only 1058 sites, with 615 at proximal promoters (+/- 500 nt from TSS) associated with genes involved in lysosome and mTOR signalling as previously reported [13 14 15 16]. Interestingly, OxPhos and autophagy [17 18] were also represented (**Figs. S6A-B**). MEME-ChIP analyses of endogenous TFE3 sites revealed enrichment only of the M/E-box motif (**Fig. S6C**). In contrast, 17-28-fold more sites were seen in HEKT cells expressing native TFE3 or PRCC-TFE3 fusions with NONO-TFE3 showing the highest number of peaks (**Fig. S6A**). MEME-ChIP revealed enrichment of the M/E-box in the TFE3 and PRCC-TFE3 expressing lines together with the SP1/KLF motif, whereas in the NONO-TFE3 expressing cells, the SP1/KLF and NFY-binding CAAT-box motifs were the

most enriched (**Fig. S6C**). Again, the M/E-box was protected at the peak centre whereas the other motifs were spread across the peaks. While endogenous TFE3 was present at only 615 proximal promoters, the ectopically expressed proteins bound much more promiscuously at promoters, most notably NONO-TFE3 (**Fig. S6A**). Thus, high nuclear accumulation of native TFE3, PRCC-TFE3 and, in particular of NONO-TFE3, in HEKT cells led to promiscuous promoter binding.

The broad genomic binding seemed inconsistent with the limited effects on gene expression seen by RNA-seq upon fusion protein silencing. It was previously reported that MYC can bind promiscuously to active promoters and stimulate mRNA synthesis [19 20]. As such an effect cannot be readily detected by standard RNA-seq, we performed EU incorporation to determine if TFE3 fusion silencing reduced nascent mRNA synthesis. In each cell line, siTFE3 reduced EU incorporation compared to the siCTR and hence reduced levels of mRNA synthesis **(Fig. 3D)**. The reduction was most prominent in the NONO-TFE3-expressing lines in particular an almost 45% reduction in UOK109 compared to the milder (15-20%) reduction in PRCC-TFE3 expressing lines. Together with the C&T results, these data indicated that TFE3 fusion proteins can both activate specific gene expression programs and, via binding to active promoters, more generally stimulate levels of mRNA synthesis.

TFE3 fusions directly regulate OxPhos and ferroptosis genes

To define the core program of TFE3-fusion driven genes, we identified ≈12 534 sites commonly bound in all 4 tRCC cell lines comprising an M/E-box of which 3900 were located in the proximal promoter (+/- 500 nucleotides from TSS, **Dataset S4**). KEGG ontology of the 3313 associated protein coding genes showed enrichment in previously defined TFE3 functions (lysosome, mTOR pathway, autophagy and mitophagy) but also cell cycle and metabolic pathways including Oxphos and ferroptosis (**Fig. 3E**). Of the 235 OxPhos signature genes

(comprising GSEA-OxPhos and KEGG-OxPhos genes **Dataset S2**), 145 were associated with the presence of TFE3-bound sites comprising an M/E-box within a distance of +/- 30kB of the TSS marked by H3K27ac (**Fig. S6D**). Among the 54 OxPhos genes down-regulated by siTFE3 in all 4 cell lines, 33 displayed a TFE3 bound site, while of the 59 genes up-regulated in the 3 modified HEK293T cells, 44 displayed TFE3 binding (**Fig. S6D)**.

Examples of TFE3 occupancy of M/E-box-containing sites at genes of mitochondrial electron transport chain complexes and the lysosomal V-ATPase in the tRCC lines are shown in **Figs. S7A-C**. Many of these genes were also bound by ectopic native TFE3 and the NONO- and PRCC-TFE3 fusions in HEKT cells along with endogenous TFE3 binding in the GFP line. For example, the COX5A and ATP6V0E1 loci displayed fusion protein binding to the same sites in the tRCC and HEKT cells (**Figs. S7B-C**). Similarly, *PPARGC1A* (PGC1A), a master regulator of mitochondrial biogenesis regulated by MITF in melanoma [21], also displayed multiple TFE3 fusion binding sites at the promoter and putative upstream and downstream regulatory elements in the tRCC lines (**Fig. S7C**). In contrast, no endogenous TFE3 was seen at the PPARGC1A locus, and only a subset of the sites seen in the tRCC lines were bound in HEKT cells expressing ectopic TFE3.

We noted that ferroptosis was represented in the core program and that several critical genes were regulated by the TFE3 fusions (**Fig. 3E**). GPX4 and the ferroptosis modulators GCLC and HMOX1 were upregulated by ectopic fusion protein expression in HEKT cells and both loci showed prominent binding of fusion proteins in the tRCC lines and HEKT cells (**Fig. S8A-B and Dataset S3**). Moreover, the GPX4 locus displayed a broad H3K27ac signal reminiscent of a super-enhancer in all 4 tRCC lines indicating that it may be a critical gene in these cells. In line with this, all 4 tRCC lines showed low IC50 values for the GPX4 inhibitor RSL3 between 2.6 nM for UOK109, and 58 nM for TF1 (**Fig. 3F**). These values were similar to that of A375 melanoma cells known to be ferroptosis sensitive and much lower than for

501Mel melanoma cells (IC50> 2 mM, not shown) reported to be ferroptosis resistant [22]. RSL3-induced cell death was efficiently rescued in the presence of the ferroptosis inhibitor ferristatin-1. These data showed that TFE3 directly regulated key ferroptosis genes in tRCC cells that consequently display marked sensitivity to GPX4 inhibition.

Human tRCC tumours retain elevated OxPhos gene expression during EMT

To investigate whether the elevated TFE3-driven OxPhos in the 4 tRCC cell lines was also seen in human patient samples, we integrated clinical and RNA-seq data of 37 TFE3-tRCC primary samples and 2 metastasis samples (from the same patient, therefore 38 patients and 39 samples) from a cohort of patients from American and French institutes and TCGA whose clinical and pathological features are summarized in **Figs. S9A-B.** This cohort comprised 66% (n=25) females and 34% (n=13) males (ratio 1.92:1 female:male), with a median age of 34 years (range: 3-65), amongst which 8 were under 18. All stages were broadly represented with 53% cases presenting stage I-II and 47% stage III-IV, with at least 10 cases already spread in lymph nodes and 1 case was poly-metastatic with two different metastatic samples collected. *SFPQ* (n=12), *PRCC* (n=12), *ASPSCR1* (n=5) were the most frequent fusion partners. The cohort also comprised the p34 subunit of general transcription factor TFIIH (GTF2H3) as a novel fusion partner of TFE3 (**Fig. S9C**). At the end of follow-up, 14 (36%) patients died with median overall survival of 47 months (range: 8.3-231.1 months).

To evaluate general differences in the gene expression signatures between tRCC and NAT, we normalized the bulk RNA-seq of 18 normal adjacent tissue (NAT) from the TCGA KIRC and the 39 TFE3-tRCC samples. 2856 genes were up-regulated in tumour samples and 2146 in NAT (**Fig. S9D-E**). Ontology analysis of genes up-regulated in tumours revealed enrichment in cell proliferation (regulation of cell activation, ribosome, mitotic cell cycle) and immune pathways (regulation of immune effector process, positive regulation of immune response and cytokine production). In contrast, genes up-regulated in NAT were enriched in

kidney structure and function (inorganic ion transmembrane transport, kidney development) and several metabolic pathways (organic hydroxy compound metabolic process, monocarboxylic acid metabolic process). Hence, transformation was associated with loss of epithelial and kidney identity and function, but gain of proliferation and immune markers.

To refine these analyses, we performed unsupervised clustering of gene expression identifying 3 main clusters, each enriched in specific fusion partners (**Fig. 4A**). Cluster 1 was enriched in PRCC-TFE3 fusions (8/12 cases, p.val=2.4e-3) with 3 of the remaining 4 in cluster 3. Cluster 2 was enriched in SFPQ- or NONO-TFE3 fusions (9/14, p.val=3.7e-4) with 4 of the remaining 5 in cluster 3 (**Fig. 4B**). SFPQ and NONO cases were combined as they belong to the same RNA-binding protein family and are known to form a protein complex[23]. Cluster 3 encompassed all 5 ASPSCR1-TFE3 fusions (enrichment p.val=2.4e-3), but comprised a majority (10 of 16) of non-ASPCR1 fusions. Hallmark GSEA analyses of genes differentially expressed between clusters revealed the mesenchymal characteristics and hot-immune profile of Cluster 3 (**Fig. 4B)**. Conversely, clusters 1-2 were more epithelial with enrichment in OxPhos and other metabolic pathways.

The immune profiles were consolidated by MCP-counter analysis showing clusters 1 and 2 to be mostly composed of cold tumours (22/23), whereas cluster 3 displayed immune infiltration (**Fig. S10A**). Similarly, use of a signature gene set confirmed the EMT gradient between clusters 1-3 (**Fig. S10B**). Combining these analyses further revealed the higher fibroblast signature score of mesenchymal tumours. Correlation with patient survival showed that cluster 3 (HR=5.84, Log-rank p.val=0.034) and fibroblast score (HR=3.46, Log-rank p.val=0.027) were strongly associated with poor survival (**Fig. 4C)**.

We next examined the OxPhos signature score using the 200 genes of the GSEA-OxPhos Hallmark pathway. Clusters 1 and 2 displayed higher scores than Cluster 3 (**Fig. 4D**). To compare the tRCC OxPhos scores to those of ccRCC, we stratified ccRCC tumours based

on our previously reported single cell RNA-seq signatures that defined an EMT gradient associated with poor survival and an OxPhos to glycolysis switch [24]. Based on deconvolution of the TCGA-KIRC collection with the ccRCC tumour cell signatures, we selected 20 tumours of the ccRCC.epi (epithelial), ccRCC.int (intermediate) and ccRCC.mes (mesenchymal) states and scored their OxPhos signatures (**Fig. 4D**). Comparison with the tRCC clusters showed that although ccRCC.epi had a comparable OxPhos score to tRCC clusters 1 and 2, tRCC tumours showed higher OxPhos score than the ccRCC.int and ccRCC.mes. Cluster 3 in particular showed a higher OxPhos score than ccRCC.mes. Thus, while OxPhos score strongly declined upon EMT in ccRCC, it remained elevated during EMT in tRCC consistent with the ability of TFE3 fusions to drive OxPhos gene expression.

EMT in tRCC tumours associates with presence of myCAFs and poor outcome

We investigated whether we could use the ccRCC tumour cell signatures to identify cell populations in tRCC. CibersortX deconvolution of the tRCC cohort showed that the intermediate ccRCC.int signature was present in almost all tumours (**Figs. 5A-B**). In contrast, cluster 3 tumours showed enrichment in ccRCC.mes, whereas ccRCC.epi was associated with clusters 1 and 2. Deconvolution with the ccRCC myofibroblast (my)CAF and antigen-presenting (ap)CAF signatures revealed enrichment of myCAFs in cluster 3 and hence strong correlation with ccRCC.mes, whereas apCAFs were more broadly associated with tumours of each cluster (**Figs. 5A-C**). Both ccRCC.mes (HR 5.06 Log-rank p=0,005) and myCAFs (HR 4.25, Log-rank p=0,005) were strongly associated with poor tRCC outcome (**Fig. 5D**).

We confirmed these findings in an independent tRCC cohort whose composition and clinical characteristics were described (**Fig. S11A** and [25]). Unsupervised clustering defined 3 main clusters, each enriched in specific fusion partners (**Fig. S11B**) with cluster 3 comprising the 9 ASPSCR1-TFE3 fusions and displaying analogous features to cluster 3 of the above-described cohort (**Fig. S11C)**. Cluster 3 showed strongest association with poor survival as did

the EMT and fibroblast scores (**Fig. S11D**). Deconvolution with the ccRCC tumour cell signatures again revealed the strong myCAF-mes association and both cell populations strongly associated with poor survival (**Figs. S11E-F**). Furthermore, scoring their OxPhos signatures again revealed that the tRCC EMT cluster 3 retained a higher OxPhos core compared to ccRCC.mes tumours (**Fig. S11G**).

The data from these 2 cohorts showed that tRCC tumours displayed a high OxPhos score that was maintained during EMT. Moreover, tRCC EMT was associated with enrichment in mesenchymal cancer cells and myCAFs that both strongly associated with poor survival.

Together, our data suggest that TFE3 tRCC represent a spectrum of epithelial to mesenchymal tumours, with high expression of oxidative phosphorylation and ferroptosis resistance driven directly by a TFE3 core program (**Fig. 6**).

Discussion

TFE3-fusion driven gene expression.

Here, we performed loss and gain of function experiments in cultured cells alongside multi-omics analyses conducted in both tRCC cell lines and patient tumors. Through this integrated and comprehensive approach, we profiled the genomic binding of TFE3 fusion proteins identifying a core set of target genes including those involved in OxPhos and ferroptosis. TFE3-fusions directly regulated OxPhos genes leading to higher functional OxPhos levels and drove GPX4 expression and ferroptosis resistance, with cells highly sensitive to RSL3-induced ferroptotic cell death. Consequently, tRCC tumours displayed elevated OxPhos scores that persisted during their EMT defining a novel metabolic subtype of renal carcinoma. Furthermore, we uncovered a correlation between EMT, the presence of mesenchymal tRCC cells and myCAFs that emerged as hallmarks of poor prognostic outcome. This association underscores the clinical relevance of EMT and the presence of myCAFs in the overall progression and outcome of tRCC.

An important observation of our study is the broad binding of NONO-TFE3 and PRCC-TFE3 over the genome. Previous studies on a limited set of tRCC lines reported only small numbers of TFE3 fusion binding sites (around 3032 sites in UOK146 and SFPQ-TFE3 xenograft lines [14], 4129 in UOK109 and 1584 in UOK120 [16]) and they provided no information on association with active H3K27ac-marked regulatory elements. These observations, obtained by ChIP-seq using antibodies distinct from those used here, are inconsistent with the abundant nuclear expression of the fusion proteins. The comprehensive Cut&Tag profiling we report here using 2 independent antibodies, identified more than 12 000 M/E-box-containing sites occupied in all 4 tRCC lines, with 3900 located in proximal promoters of genes many of which were associated with functions previously found to be regulated by native TFE3, such a lysosome and mTOR pathway, but also novel pathways pertinent to oncogenic transformation such as cell cycle, metabolism and ferroptosis.

While endogenous TFE3 bound only a restricted number of sites in HEKT cells, consistent with its lower expression and limited nuclear presence, ectopically expressed native TFE3, and the NONO- and PRCC-TFE3 fusion proteins, that accumulated in the nucleus, bound many more sites and promiscuously at promoters. In particular, the NONO-TFE3 fusion displayed broadest binding in both tRCC and HEK293T cells. The 1000 most occupied PRCC-TFE3 sites in HEKT cells and UOK120 and UOK146 tRCC cells were strongly enriched in the E/Mbox motif, indicating that most sites were directly bound. In contrast, analogous analyses of NONO-TFE3 revealed enrichment for the E/Mbox, but also promoter SP1/KLF and NFY motifs, indicating that unlike PRCC-TFE3, NONO-TFE3 bound indirectly at promoter sites with high affinity. While, this may be explained by the much higher nuclear accumulation of NONO-TFE3 in the tRCC lines, this is not the case in the HEKT cells, rather suggesting that increased indirect promoter binding is an intrinsic property of the NONO-TFE3 fusion.

Several mechanisms may account for the ability of the fusions to associate with active promoters. The NONO-SFPQ complex was previously shown to interact with the C-terminal domain (CTD) of the largest subunit of RNA polymerase II (Pol II) and bind to proximal promoters [26] [27] [28]. The NONO-TFE3 fusion protein may therefore also be recruited promiscuously to promoters in an analogous manner via the Pol II CTD. Although less is known concerning the splicing factor PRCC, TFE3 fusion partners are invariably proteins involved in RNA splicing or metabolism. It is now well established that such factors assemble on the CTD to coordinate transcription and splicing [29] [30] [31]. For example, the TFE3 partner ZC3H4 is not involved in splicing, but restriction of non-coding transcription [32] [33] [34] and was shown to be recruited to active promoters. Moreover, TFE3 can be fused with Mediator subunit MED15 or the p34 subunit (GTF2H3) of TFIIH, general transcription factors integral to the Pol II preinitiation complex. It is therefore probable that recruitment to active promoters is a general feature of TFE3 fusions. In addition, it was reported that high NONO-TFE3 accumulation may result from its oligomerization and formation of phase separated condensates [35]. The presence of the fusion partners in nuclear speckles or other phase separated structures coordinating transcription and RNA splicing/metabolism may further contribute to promiscuous TFE3-fusion binding to promoters and other regulatory elements.

Nevertheless, broad promoter binding was also seen with ectopically expressed native TFE3 indicating that while the fusion partner may contribute to this, it is not absolutely necessary. Promoter binding may therefore be mediated either through the presence of the fusion partner and/or by TFE3 tethering via SP1-family or NFY transcription factors whose motifs were abundant at TFE3-bound promoter sites. In addition, ectopically expressed native TFE3 was able to active OxPhos, although to a lesser extent than the NONO) and PRCC-TFE3 fusion. These properties of highly nuclear expressed native TFE3 may be pertinent to tRCC where TFEB is either amplified or fused with the non-coding RNA MALAT1 [8] [36] [37]. In both

situations, native TFEB accumulates in the nucleus suggesting that activation of OxPhos and/or promiscuous promoter binding may also be facets of its oncogenic function.

Here we found that mRNA synthesis was diminished upon TFE3 fusion silencing consistent with its broad promoter recruitment. Moreover, consistent with the increased propensity of NONO-TFE3 to bind active promoters, the strongest reductions in EU incorporation were seen in UOK109 and in TF1, despite its poorer transfection efficiency. It was previously reported that high MYC accumulation in cancers led to its promiscuous promoter recruitment causing transcriptional amplification [19 20]. Similarly, oncogenic RAS stimulates global mRNA synthesis when used to transform immortalized fibroblasts [38] and RAS-mediated oncogenesis is associated with increased TATA-binding protein expression and increased transcription that promote oncogenic transformation [39 40]. Together, these data suggest that global stimulation of mRNA synthesis is a feature shared by several oncogenic proteins and that contributes to oncogenic transformation. Hence TFE3 fusions may act in a bipartite manner, activating specific genes via binding to M/E-box containing regulatory elements and more generally stimulating mRNA synthesis via promoter binding.

TFE3 fusion-driven OxPhos and ferroptosis resistance as mechanisms driving tRCC tumorigenesis.

Loss and gain of function experiments revealed that TFE3 fusions directly drive a large set of OxPhos genes. Down-regulation of OxPhos gene expression correlated with reduced maximal and reserve OxPhos capacities following siTFE3 silencing, but we did not observe the reduced basal OxPhos previously reported in UOK109 cells [34, 38]. Ectopic fusion protein expression in HEK293T cells rapidly activated numerous OxPhos genes leading to increased functional OxPhos levels. Therefore, both loss and gain of function experiments converged to show how the NONO- and PRCC-TFE3-fusions directly regulated OxPhos related genes

driving high OxPhos levels in tRCC lines. This comprehensive set of genes went beyond the previously reported *PPARGC1A* and *NMRK2* genes [42 43].

These observations from cell lines were extended to two independent patient tumour cohorts. In line with the ability of TFE3 fusions to drive OxPhos gene expression and as previously suggested [44 13 45], tRCC tumours displayed globally elevated OxPhos scores compared to ccRCC. Furthermore, by stratifying ccRCC tumours of different EMT status, we showed that OxPhos score was strongly reduced during EMT in ccRCC, but maintained at higher levels in tRCC. This function of TFE3 in tumours is reminiscent of its role in metabolism and mitochondrial function in normal tissues [46]. High OxPhos has been associated with an increased propensity for oncogenic transformation and resistance to apoptosis [47 48]. Similarly, maintaining elevated OxPhos may promote tumour growth in the stressful cellular environments encountered in primary tumours and during metastatic dissemination [49]. The TFE3-related transcription factor MITF was shown to drive OxPhos in melanoma through regulation of PPARGC1A, but also the non-coding RNAs SAMMSON and LENOX [21 50 51 52]. High OxPhos in melanoma is associated with resistance to oxidative stress and resistance to MAP kinase inhibition. The fact that numerous pathways converge to regulate OxPhos further highlights the important role of this pathway in tumour development. Together these observations support the idea that TFE3 fusion driven OxPhos may be an essential aspect of the initiation, survival and progression of tRCC tumours and a mechanism shared amongst MiT family-dependent tumours.

Another mechanism that may contribute to tRCC tumorigenesis is ferroptosis resistance. Ferroptosis-related genes were found in the core program of TFE3-fusion proteins, with *GPX4*, *HMOX1*, *GCLC* and *ASCL1* upregulated by TFE3 fusion protein expression in HEKT cells. Notably, *GCLC* and *HMOX1* have been described as NFE2L2 (NRF2) targets [53 54], a pathway reported to be active in tRCC [13]. However, TFE3-fusions bound to M/E-box motifs in the

HMOX1 and *GCLC* proximal promoters and upregulated their expression identifying them as direct target genes. Similarly, the proximal promoters of the X_C-transporter system genes *SLC3A2* and *SLC7A11* also displayed TFE3-fusion binding to M/E-box motifs with *SLC7A11* expression upregulated upon fusion protein expression in HEKT cells. Accordingly, tRCC lines showed marked sensitivity to GPX4 inhibition with IC50 values in the nanomolar range similar to renal medullary carcinoma lines that we previously showed were highly sensitive to GPX4 inhibition [55]. Although NFE2L2 can regulate antioxidant and ferroptosis response in different cellular contexts, in tRCC TFE3 fusions may bypass this requirement to directly regulate key ferroptosis genes such as *GPX4* and *GCLC* promoting ferroptosis resistance and protection from oxidative stress both of which enhance tumour growth. These observations are reminiscent of those reported in melanoma where TFE3 drives GPX4 inhibitor sensitivity in MITF-low melanoma cells [22]. Direct TFE3 fusion regulation of genes involved in OxPhos and ferroptosis therefore constitute two complementary mechanisms that may contribute to tRCC tumorigenesis. Moreover, the observation of ferroptosis resistance in tRCC underlines this process as a common mechanism for RCC development [56].

EMT and myCAFs, markers of poor outcome common to tRCC and ccRCC.

Analyses of the tRCC cohorts revealed that EMT and presence of myCAFs both associated with poor outcome, characteristics shared with ccRCC [24]. In each tRCC cohort, we stratified tumours that differed in EMT status, hot-immune microenvironment and presence of CAFs. As previously observed [25], ASPSCR1-TFE3 tumours displayed a strong propensity for EMT, but tumours with other fusion partners also underwent EMT. Interestingly, tumours with PRCC or SFPQ fusions displayed either epithelial or mesenchymal signatures highlighting the variability among their phenotypes. EMT of tRCC cancer cells was further consolidated by deconvolution with signatures for epithelial and mesenchymal ccRCC cancer cells. Tumours with EMT signatures were enriched in mesenchymal cancer cells showing that the bulk EMT

signature was not only due to presence of fibroblasts or other components of the TME. Similarly, deconvolution revealed that EMT tumours were enriched in myCAFs and that enrichment in both mesenchymal tumour cells and myCAFs were strongly associated with poor survival. Thus, despite the distinct oncogenic mechanisms, both ccRCC and tRCC tumours display EMT and infiltration by myCAFs that constitute hallmarks of poor disease outcome. Future studies will clarify the similarities and differences in the myCAF across RCC subtypes and whether this could be used to personalize treatments of patients using immune checkpoint inhibitors [57 58].

Methods

Cell Culture

UOK109, UOK120, UOK121, UOK112 and UOK146 were generous gift from Dr Martson Linehan (NIH, Bethesda, USA) while TF1 line was a generous gift from Dr Gilles Pagès (Nice, France). These cell lines were grown in DMEM medium supplemented with glucose (4.5g/L), 10% heat-inactivated Foetal Calf Serum (FCS), Non-essential amino acid (AANE) and 1% penicillin/streptomycin. The remaining cell lines were purchased from ATCC. The embryonic kidney HEK293T cell line and the derived lines expressing ectopic TFE3 fusions as well as UOK121, UOK112 and RCC4 cells were grown in DMEM medium supplemented with glucose (1g/L), 10% FCS and 1% penicillin/streptomycin. The primary kidney cell line RPTEC was grown in DMEM/F12 medium supplemented with 2.5mM L-Glutamine, 15mM HEPES, hTERT Immortalized RPTEC growth kit-supplement A&B (ATCC ACS-4007), gentamycin (40µg/mL) and G418 (100µg/mL). 786-O ccRCC cells were grown in RPMI 1640 medium supplemented with glucose (2.5g/L), HEPES (10mM), 10% FCS, sodium pyruvate (1mM) and gentamycin (40µg/mL). A-498 ccRCC cells were grown in MEM medium (LifeTechnologies 31095-029) supplemented with 10% heat-inactivated FCS and gentamycin

(40µg/mL). The papillary carcinoma renal cell line ACHN was grown in MEM medium (ATC 30-2003) supplemented with 10% FCS and gentamycin (40µg/mL). All cells were cultured at 37°C, 5% CO_2.

Cell line transfection with siRNA

For siRNA knockdown experiments, 400 000 cells were plated in 6-well plates 18 hours before transfection. Transfection was performed in OPTI-MEM medium using lipofectamine RNAiMAX (13778150 – Invitrogen) with 25nM siRNA (mix of 3 individual siRNA for knockdown of TFE3 – J-009363 -06, -08, -09, or with a pool of 4 non-targeting siRNA as control – D-0018-10 – Dharmacon). After 7 hours of incubation, OPTI-MEM was replaced by complete medium. siRNAs sequences are listed in the Table S1.

Plasmid production, lentiviral particle production, cell line transduction and expression

TFE3, NONO-TFE3 and PRCC-TFE3 cDNAs were synthesized by GenScript and subsequently cloned into the all-in-one doxycycline inducible lentiviral vector pCW57-GFP-P2A-MCS vector (Addgene plasmid #71783) in place of GFP. Lentiviral particles were produced to express independently each of the 3 genes of interest or GFP control by transfection of HEK293T cells with packaging plasmids. Lentiviral particles were purified by filtration and ultracentrifugation and resuspended in PBS. After titration, HEK293T cells were infected at multiplicity of infection of 1 using polybrene and selected by puromycin addition to the media (1μg/mL). After establishment of the stable cell lines, expression of the proteins of interest was induced by adding of Doxycycline (Dox) in the medium (10µg/mL).

RNA extraction and quantitative PCR

Total mRNA isolation was performed using Trizol (TR 118) and isopropanol precipitation. RNA was then treated with DNAseI following the TurboDNAse kit instructions (AM1907 – ThermoFisher) and 1μg of RNA was reversed transcribed using SuperScript IV (18090050 – ThermoFisher) following manufacturer instructions. qPCR (program: 95°C,

15min; (95°C, 10s; 55°C, 15s; 72°C, 10s) x60; (95°C, 5s; 70°C, 1min05; 95°C, 5 min) x1; cool down) was performed using SYBR Green I (Roche) and monitored by a LightCycler 480 (Roche). Target gene expression was normalized using the geometric means of *TBP*, *HMBS*, *GAPDH*, *RPLP0* as reference genes. Primers for RT-qPCR were designed using the OligoAnalyzer™Tool from IDT and are listed in Table S2.

Total protein extraction

Whole cell extracts were prepared by 4 freeze-thaw cycles in LSDB 0.5M buffer (0.5M KCl, 25mM Tris pH7.9, 10% glycerol v/v, 0.05% NP-40 v/v, 16mM DTT and protease inhibitor cocktail, 1861280 – Thermo Fisher). After 20 minutes on ice, extracts were centrifuged for 10 minutes at 13 000g, 4°C and supernatant was retrieved.

Differential extraction of nuclear and cytoplasmic proteins

Protein extracts from nuclear and cytoplasmic compartments were prepared using manual lysis and sucrose buffer. Briefly, cells were resuspended in hypotonic buffer (1mL buffer / g of cells – 10mM Tris pH7.65, 1.5mM $MgCl_2$, 10mM KCl), incubated on ice for 5 min and transferred to a loose Dounce. After 15 strokes, sucrose buffer (0.33mL/g cells – 20mM Tris pH7.65, 15mM KCl, 60mM NaCl, 0.34M sucrose) and PMSF (0.2mM) were added to the lysed solution and centrifuged for 10min at 4500g, 4°C. The supernatant was recovered (cytosolic extract) and the pellet resuspended in sucrose buffer (1mL/g cells). Hypertonic buffer (20mM Tris pH7.65, 25% glycerol, 1.5mM $MgCl_2$, 0.2mM EDTA, 900mM NaCl) was added dropwise under slight agitation (0.35mL/g cells), tubes were incubated for 30min at 4°C on a wheel and centrifuged for 10min at 4700g, 4°C. The supernatant formed the soluble nuclear extract.

Immuno-blots

Proteins were quantified using the Bradford protein quantification assay (BioRad) and 20μg of extract were used to perform SDS-polyacrylamide gel electrophoresis. Proteins were

transferred to a nitrocellulose membrane. Membranes were incubated overnight at 4°C with primary antibody diluted in PBS + 5% dry-fat milk + 0,01% Tween-20. After washing steps, membranes were incubated with HRP-conjugated secondary antibodies for 1 hour at room temperature and revealed using the ECL detection system (GE Healthcare). Antibodies and used dilutions are listed in Table S3.

Colony forming analyses by Crystal violet staining

Colony formation was assessed by plating 5 000 cells in 6-well plates, incubating them for 14 days and finally fixing in 4% paraformaldehyde and staining with 0,05% Crystal Violet solution (Sigma Aldrich). Modified HEK293T lines used for Dox-inducible gain of function experiments were plated on poly-D-lysine pre-coated dishes and Dox was renewed every 48 hours.

RNA-sequencing and analysis

Cells were harvested by scraping 72 hours after siRNA transfection and total mRNA was extracted with Trizol as described above. For HEKT cells, RNA was prepared 24 hours after Doxycycline (Dox) addition. Following QC and library preparation, RNA-seq was performed on an Illumina Hiseq4000 as 2*100bp paired end sequencing following Illumina's instructions. After sequencing raw reads were pre-processed in order to remove adapter and low-quality sequences (Phred quality score below 20) using cutadapt version 1.10 and reads shorter than 40 bases were discarded. Reads were mapped to rRNA sequences using bowtie version 2.2.8 and matching reads removed. Remaining reads were then mapped onto the hg19 assembly of Homo sapiens genome using STAR version 2.5.3a. Gene expression quantification was performed from uniquely aligned reads using htseq-count version 0.6.1p1, with annotations from Ensembl version 75 and "union" mode. Only non-ambiguously assigned reads were retained for further analyses. Read counts were normalized across samples with the median-of-ratios method. Comparisons of interest were performed using the Wald test for differential

expression and implemented in the Bioconductor package DESeq2 version 1.16.1. Genes with high Cook's distance were filtered out and independent filtering based on the mean of normalized counts was performed. P-values were adjusted for multiple testing using the Benjamini and Hochberg method. Deregulated genes were defined as genes with log2(fold-change) >1 or <-1 and adjusted p-value <0.05. Gene set enrichment analyses were done with the GSEA software v3.0 using the hallmark gene sets of Molecular Signature Database v6.2. Gene Ontology analysis was performed using the Database for Annotation, Visualization and Integrated Discovery (http://david.abcc.ncifcrf.gov/). Gene list intersections were computed and Venn diagrams represented using the web tool Venny (https://bioinfogp.cnb.csic.es/tools/venny/). Gene set variation analysis (GSEA) was computed using the Bioconductor R package GSVA v1.48.3.

Measure of Oxygen Consumption Rate (OCR) in living cells

OCR in living cells was measured using the MitoStress kit and the XF96 extracellular analyser (Agilent) following manufacturer's instructions. Cells were seeded 48 hours prior to measurement in SeaHorse microplates (Agilent) in order to have confluent cells on the day of measurement: 30 000 cells per well for translocation cell lines, 40 000 cells for Dox-inducible HEK293T lines, 10 000 cells for 786-O and 20 000 cells for UOK121. Dox-inducible HEK293T cells were treated with Dox 24 hours prior to measurement. For siRNA-mediated knockdown, 30 000 UOK109 cells were seeded per well, after 7 hours of incubation with siRNA and 65 hours prior to measurement, whereas 20 000 cells were seeded for TF1, UOK120, UOK146. For each line, 6 wells were considered for technical replicates per experiment and up to 5 biological replicates were performed. The day before measurement, the cartridge was hydrated. One hour before measurement, medium on cells was changed for XF base medium supplemented with 1mM pyruvate, 2mM glutamine and 10mM glucose and cells were incubated at 37°C with no CO_2. After calibration of the cartridge, cells were sequentially exposed to 1μM oligomycin, 1μM carbonyl cyanide-4-(trifluorome-thoxy)-phenylhydrazone

(FCCP), and 0.5μM rotenone/antimycin A, with 13 min between each drug. After measurement, cells were fixed with 4% PFA, permeabilized with 0.2% Triton and stained with DAPI (1μg/μL). Number of cells per well was determined by microscopy at the IGBMC High Throughput Screening Facility and used to normalize obtained measurements per well. Calculation of basal, maximal and reserve capacity were performed as defined in the Agilent User Guide.

ChiP-seq and Cut&TAG

For H3K27ac chromatin immunoprecipitation, cells were grown in 15cm petri dishes and fixed with 0,4% PFA for 10min at room temperature with agitation. Crosslinking was quenched by adding glycine (2M, pH8) for 10min with agitation. Fixed cells were washed once with PBS, harvested by scraping, pelleted and resuspended in lysis buffer (2-times pellet volume – 50mM TrisHCl pH8, 1% SDS, 10mM EDTA, 0,1M PMSF, protease inhibitor cocktail). Lysates were transferred to Covaris tubes and sonicated in a Covaris sonicator to obtain DNA fragments (median size 200-500 bp). After sonication, lysates were centrifuged at 13 000g, 4°C for 10min. Chromatin sonication was verified on agarose gels after decrosslinking (overnight incubation at 65°C with 0.3M NaCl, RNAseA and 1h incubation with proteinase K at 42°C) and phenol-chloroform extraction. 100μg of chromatin were diluted with ChIP dilution buffer (16.7mM Tris HCl pH8, 167nM NaCl, 1.2mM EDTA, 1.1% Triton X-100, 0.01% SDS) and precleared with Protein G DNA magnetic beads (30μL/mL lysate) for 1h, 4°C. After bead removal, chromatin extracts were incubated with anti-H3K27ac (1μg/20μg of chromatin) at 4°C, overnight. To recover antibody-chromatin complexes, Protein G DNA magnetic beads were added to each sample and incubated at 4°C for 1h. Beads were then washed with 4 different buffers, two times each (Low Salt Buffer: 20mM Tris HCL pH8, 150mM NaCl, 2mM EDTA, 1% Triton X-100, 0.1% SDS; High Salt Buffer: 20mM Tris HCL pH8, 500mM NaCl, 2mM EDTA, 1% Triton X-100, 0.1% SDS; LiCl Buffer: 10mM Tris HCl pH8, 1mM EDTA,

1% sodium deoxycholate, 1% NP40, 0.25mM LiCl; TE Buffer: 10mM Tris HCl pH8, 1mM EDTA). Finally, beads were re-suspended twice in DNA elution buffer (0.1M $NaHCO_3$, 1%SDS) and incubated 15min at room temperature. Decrosslinking and phenol-chloroform extraction were then performed and extracted DNA was resuspended in water. After QC and library preparation, DNA was sequenced on Illumina HiSeq 4000 sequencer as 1*50bp single-read following Illumina's instructions.

For Cut&TAG, cells were plated in 10 cm petri-dish for 48h and harvested using CellStripper solution and washed 2 times in PBS 1X. 500 000 cells were used for Cut&TAG experiments following the manufacturer's instructions (Cut&TAG-IT™ Assay kit – n°53160 – ActiveMotif). Libraries were prepared using the Nextera™-Compatible Multiplex Primers (96-plex – n°53155 – ActiveMotif). Libraries were verified on a BioAnalyzer before 2 rounds of purification using SPRI beads as described in the Cut&TAG kit. Antibodies used are listed in Table S3.

Analysis of ChIP-seq and Cut&TAG

Following sequencing, reads were mapped to the Homo sapiens genome assembly hg19 using Bowtie with the following arguments: -m 1 --strata --best -y -S -l 40 -p 2. Peak detection was performed using the MACS software v1.4.3 for transcription factors and v2.1.1 for chromatin marks. Peaks were annotated with the 'annotatePeaks' command from HOMER v4.11 using the GTF annotation file from ENSEMBL v75 (http://homer.ucsd.edu/homer/ngs/annotation.html). Global clustering analyses with quantitative comparisons and representations of read density heatmaps were performed using seqMINER. Gene ontology analyses from peak annotations were performed with the Bioconductor R package clusterProfiler v4.8.2 and the metascape web tool (https://metascape.org). Motif discovery from ChIP-seq peak sequences was performed using the MEME CHIP and RSAT peak-motifs algorithms (http://rsat.sb-roscoff.fr/peak-

motifs_form.cgi). Peak intersections were computed using bedtools v2.26.0 and for multiple samples, the R package DiffBind v3.8.4. Visualization of ChIP-seq signal at specific gene loci of interest was achieved using the UCSC genome browser (https://genome.ucsc.edu/).

RNA-sequencing and analysis of patient tumour samples

RNA sequencing for TFE3 tRCC was available for 39 samples from 38 patients (one patient presented with metastases resulting in two samples) including in house cohort of 26 samples and 13 samples from TCGA KIRC and KIRP cohorts. Identification of fusion transcripts for 17 of those samples have been previously reported [59] [60] and nine samples were novel. Library preparation, sequencing and fusion transcript detection for those novel samples was performed as previously described [60]. After sequencing, raw read counts were adjusted for batch-effect correction using ComBat-seq by providing the sequencing batch as the 'batch' argument. For analyses requiring integration with TCGA-KIRC samples, an additional covariate specifying the type of sample (tRCC, normal adjacent tissue or ccRCC) was provided as the 'group' argument. The adjusted raw-count matrices were normalized by sequencing depth using DESeq2 size-factors and then gene-counts were divided by median transcript lengths.

Consensus clustering of TFE3-fusion samples was performed using the R package ConsensusClusterPlus v3.17 following standard procedure. In short, matrices are filtered in order to keep only coding genes based on their biotype annotation. The 5000 most variable genes were retained with the mad() function and the matrices were median centered with the sweep(), apply() and median() functions. Consensus clustering was done with the ConsensusClusterPlus() function using base parameters. The appropriate numbers of clusters were chosen based on the curve of cumulative distribution function. Differential gene expression analyses between the different groups were done with DESeq2 with functional analyses and visualization performed as described in the previous section for cellular models.

Translocation tumour samples were subjected to deconvolution analysis using the R-package MCP-counter v1.2.0. Then, hierarchical clustering was performed based on the MCP-counter population scores using the hclust() function with "ward.D2" linkage in order to define "hot" and "cold" tumour groups.

Translocation tumour samples were scored according to their mesenchymal/epithelial signature ratios in the following way: epithelial and mesenchymal genes derived from ccRCC samples described in Liang et al. [61]were subjected to unsupervised clustering using tRCC samples then these genes were assigned into mesenchymal and epithelial categories based on their expression patterns in tRCC in order to adapt the original signatures. Some genes such as *VEGFA* and *ANGPTL4* showed different expression patterns in tRCC compared to what was described in ccRCC and were re-assigned to their proper categories while some genes such as *CA9* had no clear expression patterns in tRCC and were removed. Lastly, mesenchymal genes and proximal tubule markers identified from single-cell analyses were added to complete the new mesenchymal and epithelial signatures in order to have the 22 representative genes in each category. The 'SignatureRatio' value was computed as the geometric mean of the mesenchymal signature divided by the geometric mean of the epithelial signature.

Deconvolution of tRCC samples using the ccRCC single cell RNA-seq signatures we previously described was performed using CIBERSORTx algorithm [24]. To stratify epithelial, intermediate and mesenchymal ccRCC samples, tumor samples from the TCGA-KIRC were ordered by the ccRCC.epi/ccRCC.mes ratio of their CIBERSORTx score, then the top 20 were chosen as epithelial, the bottom 20 as mesenchymal and the 20 around the median as intermediate.

Scoring of a considered list of genes to determine patient survival was defined as the geometrical mean of representative genes of the transcriptional signature.

Patient survival was computed in R using packages survival v3.2 and survminer v0.4.9. Patients were stratified using the surv_cutpoint() function and Kaplan–Meier curves were

represented with the survfit() and ggsurvplot() functions. Hazard ratios were determined by univariate Cox proportional-hazards models with the "coxph()" function.

Labelling nascent RNA with 5-ethynyluridine (EU)

EU incorporation experiments were conducted using the Click-iT™ RNA Alexa Fluor™ 594 Imaging kit from Invitrogen (C10330), following the supplier's recommendations. Cells were transfected with siCTR or siTFE3 in 6-well plates before replating 25000 cells in 8-well cell culture slides (CCS8 – Mattek) and growing for 24h. Fresh media containing 1 mM of the cell-permeable uridine analog, 5-ethynyluridine (EU) and a final concentration of 50 ng/mL Actinomycin D were added for one hour prior to fixation. Fixation was performed with a 3.7% Formaldehyde solution in PBS for 15 minutes, followed by permeabilization with a 0.5% Triton-X PBS solution for an additional 15 minutes before continuing with the EU labelling in accordance with the protocol's instructions. After one wash step with PBS 1x, cells were fixed with 3.7% formaldehyde for 15min at RT, washed once with PBS and permeabilized with 0.5% Triton X-100 in PBS 1x for 15min and washed again with PBS. Cells were then incubated with Click-IT® reaction cocktail as described in the kit for 30 min at RT protected from light. The cell nuclei were counterstained with Hoechst 33342. After two washes in PBS 1x, microscope slides were mounted using DAPI-ProLongGold (P36935 – ThermoFisher). Images were capture with a SP8-X confocal microscope and the EU fluorescence signal from the nucleus was quantified using the Hoechst signal as a mask for determining the mean fluorescence of the EU signal in each nucleus by analyses using a FlowJo macro program.

Treatment with RSL3 and determination of IC50

10 000 cells were plated in 96-well plate and cultured overnight. Cells were treated with 1, 5, 10, 25, 50, 100, or 250 nM of RSL3 with or without 1uM ferrostatin-1 (SelleckChem, #S7243) and cultured for 48 hours. Each condition was performed in triplicate. Complete medium was replaced by a solution of 1:1 complete medium/PrestoBlue™ (A13261 –

Invitrogen) and incubated for 1h at 37°C, 5% CO_2. Viability was then evaluated by measuring the absorbance at 590 nm. Dose response curves and the half maximal inhibitory concentration (IC50) were calculated using GraphPad Prism software.

Statistics.

The statistical tests used in each analysis, mainly paired t-test, 1-way Anova (with Dunett's correction) or Wilcoxon test, are described in the corresponding figure legends with the p-values.

Data Availability.

The sequencing data reported in this study as available as SuperSeries GSE268093 in the GEO data base.

Table S1 – siRNA sequences

siRNA	Sequence (5' -> 3')
siCTR - pool	UGGUUUACAUGUCGACUAA, UGGUUUACAUGUUGUGUGA, UGGUUUACAUGUUUUCUGA, UGGUUUACAUGUUUUCCUA
siTFE3 #6	GGAAUCUGCUUGAUGUGUA
siTFE3 #8	CGCAGGCGAUUCAACAUUA
siTFE3 #9	CAGAGCAGCUGGACAUUGA

Table S2 – Primers sequences – Primers used for RT-qPCR to verify TFE3 expression level in cell lines

Primer name	Sequence (5' -> 3')
HMBS_F	GGCAATGCGGCTGCAA
HMBS_R	GGGTACCCACGCGAATCAC
GAPDH_F	ACAACTTTGGTATCGTGGAAGG
GAPDH_R	GCCATCACGCCACAGTTTC

RPLP0_F	AGTGTTCTGGGCTGGCACA
RPLP0_R	GAAACTGCTGCCTCATATCC
TFE3_F	GCCATCACTGTCAGCAACTC
TFE3_R	GATGAGAGTGCCCAGTTCCT

Table S3 – Used antibodies for Western-blot and Immunofluorescence analysis

Target	**Host**	**Application**	**Dilution**	**Reference**
TFE3	Rabbit Rabbit	WB; Cut&Tag (tRCC) Cut&Tag (UOK109, HEKT)	1/2500; 1µg 1µg	HPA-023881 (Sigma) Lot. 000009169 Ab93808 (Abcam) Lot 1003520-27
VCL	Mouse	WB	1/1000	V4505 (Sigma Aldrich) Lot 099M4850V
BRG1	Rabbit	WB	1/10 000	Ab110641 (Abcam) Lot : 1000647-1
GAPDH	Rabbit	WB	1/1000	In house
Histone H3	Rabbit	WB	1/1000	Ab1791 (Abcam) Lot 150891-1
H3K27ac	Rabbit	ChIP-seq	10µg	39133 (ActiveMotif) Lot 31521015-13
IgG	Rabbit	Cut&Tag Control	10µg	Ab171870 ((Abcam) Lot 3353004-2

Bibliography

1. Raben, N. & Puertollano, R. TFEB and TFE3: Linking Lysosomes to Cellular Adaptation to Stress. *Annu. Rev. Cell Dev. Biol.* **32**, 255–278 (2016).
2. Bakouny, Z. *et al.* Integrative molecular characterization of sarcomatoid and rhabdoid renal cell carcinoma. *Nat. Commun.* **12**, 808 (2021).
3. Caliò, A., Segala, D., Munari, E., Brunelli, M. & Martignoni, G. MiT Family Translocation Renal Cell Carcinoma: from the Early Descriptions to the Current Knowledge. *Cancers* **11**, (2019).
4. Ellati, R. T. *et al.* Clinicopathologic Features of Translocation Renal Cell Carcinoma. *Clin. Genitourin. Cancer* **15**, 112–116 (2017).
5. Moch, H., Cubilla, A. L., Humphrey, P. A., Reuter, V. E. & Ulbright, T. M. The 2016 WHO Classification of Tumours of the Urinary System and Male Genital Organs-Part A: Renal, Penile, and Testicular Tumours. *Eur. Urol.* **70**, 93–105 (2016).
6. Geller, J. I. *et al.* Characterization of adolescent and pediatric renal cell carcinoma: A report from the Children's Oncology Group study AREN03B2. *Cancer* **121**, 2457–2464 (2015).
7. Sukov, W. R. *et al.* TFE3 rearrangements in adult renal cell carcinoma: clinical and pathologic features with outcome in a large series of consecutively treated patients. *Am. J. Surg. Pathol.* **36**, 663–670 (2012).
8. Kauffman, E. C. *et al.* Molecular Genetics and Cellular Characteristics of TFE3 and TFEB Translocation Renal Cell Carcinomas. *Nat. Rev. Urol.* **11**, 465–475 (2014).
9. Grépin, R. *et al.* The Relevance of Testing the Efficacy of Anti-Angiogenesis Treatments on Cells Derived from Primary Tumors: A New Method for the Personalized Treatment of Renal Cell Carcinoma. *PLoS ONE* **9**, e89449 (2014).
10. Clark, J. *et al.* Fusion of splicing factor genes PSF and NonO (p54 nrb) to the TFE3 gene in papillary renal cell carcinoma. *Oncogene* **15**, 2233–2239 (1997).
11. Sidhar, S. The t(X;1)(p11.2;q21.2) translocation in papillary renal cell carcinoma fuses a novel gene PRCC to the TFE3 transcription factor gene. *Hum. Mol. Genet.* **5**, 1333–1338 (1996).

12. Suske, G. NF-Y and SP transcription factors - New insights in a long-standing liaison. *Biochim. Biophys. Acta Gene Regul. Mech.* **1860**, 590–597 (2017).

13. Bakouny, Z. *et al.* Integrative clinical and molecular characterization of translocation renal cell carcinoma. *Cell Rep.* **38**, 110190 (2022).

14. Damayanti, N. P. *et al.* Therapeutic targeting of TFE3/IRS-1/PI3K/mTOR axis in translocation renal cell carcinoma. *Clin. Cancer Res. Off. J. Am. Assoc. Cancer Res.* **24**, 5977–5989 (2018).

15. Perera, R. M., Di Malta, C. & Ballabio, A. MiT/TFE Family of Transcription Factors, Lysosomes, and Cancer. *Annu. Rev. Cancer Biol.* **3**, 203–222 (2019).

16. Yin, X. *et al.* TFE3 fusions escape from controlling of mTOR signaling pathway and accumulate in the nucleus promoting genes expression in Xp11.2 translocation renal cell carcinomas. *J. Exp. Clin. Cancer Res. CR* **38**, 119 (2019).

17. Settembre, C. *et al.* TFEB Links Autophagy to Lysosomal Biogenesis. *Science* **332**, 1429–1433 (2011).

18. Pastore, N. *et al.* Nutrient-sensitive transcription factors TFEB and TFE3 couple autophagy and metabolism to the peripheral clock. *EMBO J.* **38**, (2019).

19. Lin, C. Y. *et al.* Transcriptional Amplification in Tumor Cells with Elevated c-Myc. *Cell* **151**, 56–67 (2012).

20. Nie, Z. *et al.* c-Myc Is a Universal Amplifier of Expressed Genes in Lymphocytes and Embryonic Stem Cells. *Cell* **151**, 68–79 (2012).

21. Vazquez, F. *et al.* PGC1α Expression Defines a Subset of Human Melanoma Tumors with Increased Mitochondrial Capacity and Resistance to Oxidative Stress. *Cancer Cell* **23**, 287–301 (2013).

22. Dias, D., Louphrasitthiphol, P. & Goding, C. R. TFE3 promotes ferroptosis in melanoma. *Pigment Cell Melanoma Res.* **37**, 286–290 (2024).

23. Knott, G. J., Bond, C. S. & Fox, A. H. The DBHS proteins SFPQ, NONO and PSPC1: a multipurpose molecular scaffold. *Nucleic Acids Res.* **44**, 3989–4004 (2016).

24. Davidson, G. *et al.* Mesenchymal-like Tumor Cells and Myofibroblastic Cancer-Associated Fibroblasts Are Associated with Progression and Immunotherapy Response of Clear Cell Renal Cell Carcinoma. *Cancer Res.* **83**, 2952–2969 (2023).
25. Sun, G. *et al.* Integrated exome and RNA sequencing of TFE3-translocation renal cell carcinom. (2021) doi:10.21203/rs.3.rs-296261/v1.
26. Lim, Y. W., James, D., Huang, J. & Lee, M. The Emerging Role of the RNA-Binding Protein SFPQ in Neuronal Function and Neurodegeneration. *Int. J. Mol. Sci.* **21**, 7151 (2020).
27. Emili, A. *et al.* Splicing and transcription-associated proteins PSF and p54nrb/nonO bind to the RNA polymerase II CTD. *RNA N. Y. N* **8**, 1102–1111 (2002).
28. Kameoka, S., Duque, P. & Konarska, M. M. p54(nrb) associates with the 5' splice site within large transcription/splicing complexes. *EMBO J.* **23**, 1782–1791 (2004).
29. Saldi, T., Cortazar, M. A., Sheridan, R. M. & Bentley, D. L. Coupling of RNA polymerase II transcription elongation with pre-mRNA splicing. *J. Mol. Biol.* **428**, 2623–2635 (2016).
30. Custódio, N. & Carmo-Fonseca, M. Co-transcriptional splicing and the CTD code. *Crit. Rev. Biochem. Mol. Biol.* **51**, 395–411 (2016).
31. Shenasa, H. & Bentley, D. L. Pre-mRNA splicing and its cotranscriptional connections. *Trends Genet. TIG* **39**, 672–685 (2023).
32. Hughes, A. L. *et al.* A CpG island-encoded mechanism protects genes from premature transcription termination. *Nat. Commun.* **14**, 726 (2023).
33. Estell, C. *et al.* A restrictor complex of ZC3H4, WDR82, and ARS2 integrates with PNUTS to control unproductive transcription. *Mol. Cell* **83**, 2222-2239.e5 (2023).
34. Rouvière, J. O. *et al.* ARS2 instructs early transcription termination-coupled RNA decay by recruiting ZC3H4 to nascent transcripts. *Mol. Cell* **83**, 2240-2257.e6 (2023).
35. Wang, B. *et al.* The positive regulation loop between NRF1 and NONO-TFE3 fusion promotes phase separation and aggregation of NONO-TFE3 in NONO-TFE3 tRCC. *Int. J. Biol. Macromol.* **176**, 437–447 (2021).

36. Napolitano, G. & Ballabio, A. TFEB at a glance. *J. Cell Sci.* **129**, 2475–2481 (2016).

37. Argani, P. *et al.* TFEB-amplified Renal Cell Carcinomas: An Aggressive Molecular Subset Demonstrating Variable Melanocytic Marker Expression and Morphologic Heterogeneity. *Am J Surg Pathol* **40**, 1484–1495 (2016).

38. Kotsantis, P. *et al.* Increased global transcription activity as a mechanism of replication stress in cancer. *Nat. Commun.* **7**, 13087 (2016).

39. Johnson, S. A. *et al.* Increased expression of TATA-binding protein, the central transcription factor, can contribute to oncogenesis. *Mol Cell Biol* **23**, 3043–51. (2003).

40. Johnson, S. A., Mandavia, N., Wang, H. D. & Johnson, D. L. Transcriptional regulation of the TATA-binding protein by Ras cellular signaling. *Mol Cell Biol* **20**, 5000–9 (2000).

41. Wang, B. *et al.* PRCC-TFE3 fusion-mediated PRKN/parkin-dependent mitophagy promotes cell survival and proliferation in PRCC-TFE3 translocation renal cell carcinoma. *Autophagy* **0**, 1–19 (2020).

42. Chen, Y. *et al.* Up-regulation of NMRK2 mediated by TFE3 fusions is the key for energy metabolism adaption of Xp11.2 translocation renal cell carcinoma. *Cancer Lett.* **538**, 215689 (2022).

43. SALMA, N., SONG, J. S., ARANY, Z. & FISHER, D. E. Transcription Factor Tfe3 Directly Regulates Pgc-1alpha in Muscle. *J. Cell. Physiol.* **230**, 2330–2336 (2015).

44. Qu, Y. *et al.* Proteogenomic characterization of MiT family translocation renal cell carcinoma. *Nat. Commun.* **13**, 7494 (2022).

45. TCGA, N. COMPREHENSIVE MOLECULAR CHARACTERIZATION OF CLEAR CELL RENAL CELL CARCINOMA. *Nature* **499**, 43–49 (2013).

46. Pastore, N. *et al.* TFE3 regulates whole-body energy metabolism in cooperation with TFEB. *EMBO Mol. Med.* **9**, 605–621 (2017).

47. Bonnay, F. *et al.* Oxidative Metabolism Drives Immortalization of Neural Stem Cells during Tumorigenesis. *Cell* **182**, 1490-1507.e19 (2020).

48. Spurlock, B. *et al.* Fine-tuned repression of Drp1-driven mitochondrial fission primes a 'stem/progenitor-like state' to support neoplastic transformation. *eLife* **10**, e68394 (2021).
49. Bergers, G. & Fendt, S.-M. The metabolism of cancer cells during metastasis. *Nat. Rev. Cancer* **21**, 162–180 (2021).
50. Haq, R. *et al.* Oncogenic BRAF regulates oxidative metabolism via PGC1alpha and MITF. *Cancer Cell* **23**, 302–15 (2013).
51. Leucci, E. *et al.* Melanoma addiction to the long non-coding RNA SAMMSON. *Nature* **531**, 518–22 (2016).
52. Gambi, G. *et al.* The lncRNA LENOX interacts with RAP2C to regulate metabolism and promote resistance to MAPK inhibition in melanoma. *Cancer Res.* CAN-22-0959 (2022) doi:10.1158/0008-5472.CAN-22-0959.
53. Yan, R. *et al.* NRF2, a Superstar of Ferroptosis. *Antioxid. Basel Switz.* **12**, 1739 (2023).
54. Yang, Z. *et al.* ACTL6A protects gastric cancer cells against ferroptosis through induction of glutathione synthesis. *Nat. Commun.* **14**, 4193 (2023).
55. Vokshi, B. H. *et al.* SMARCB1 regulates a TFCP2L1-MYC transcriptional switch promoting renal medullary carcinoma transformation and ferroptosis resistance. *Nat. Commun.* **14**, 3034 (2023).
56. Yang, L., Fan, Y. & Zhang, Q. Targeting ferroptosis in renal cell carcinoma: Potential mechanisms and novel therapeutics. *Heliyon* **9**, e18504 (2023).
57. Alhalabi, O. *et al.* Immune Checkpoint Therapy Combinations in Adult Advanced MiT Family Translocation Renal Cell Carcinomas. *The Oncologist* **28**, 433–439 (2023).
58. Boilève, A. *et al.* Immune checkpoint inhibitors in MITF family translocation renal cell carcinomas and genetic correlates of exceptional responders. *J. Immunother. Cancer* **6**, 159 (2018).
59. Classe, M. *et al.* Incidence, clinicopathological features and fusion transcript landscape of translocation renal cell carcinomas. *Histopathology* **70**, 1089–1097 (2017).

60. Malouf, G. G. *et al.* Next-generation sequencing of translocation renal cell carcinoma reveals novel RNA splicing partners and frequent mutations of chromatin-remodeling genes. *Clin Cancer Res* **20**, 4129–40 (2014).

61. Liang, J. *et al.* The Correlation Between the Immune and Epithelial-Mesenchymal Transition Signatures Suggests Potential Therapeutic Targets and Prognosis Prediction Approaches in Kidney Cancer. *Sci. Rep.* **8**, 6570 (2018).

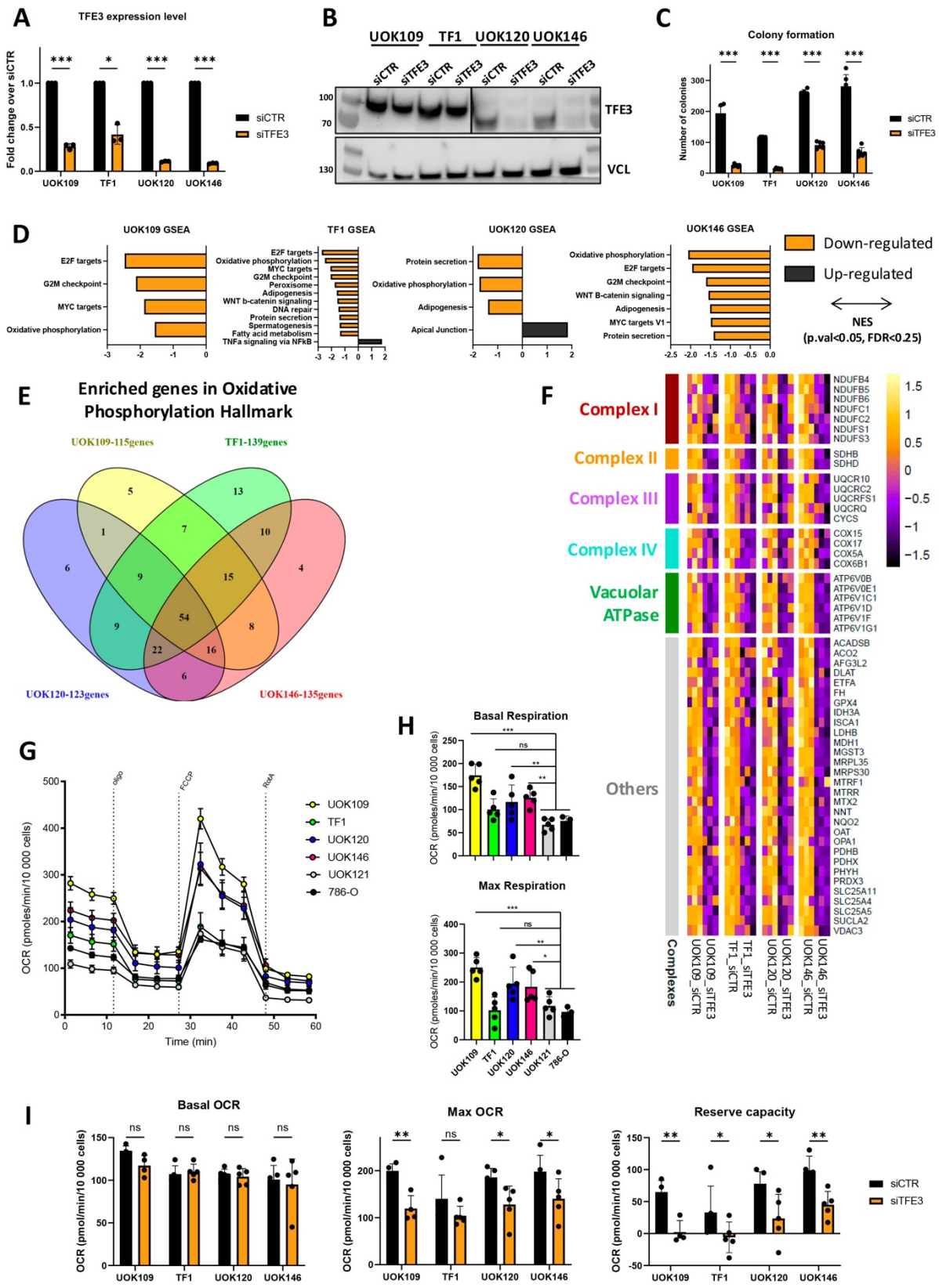
A
TFE3 expression level
Fold change over siCTR
siCTR
siTFE3
UOK109
TF1
UOK120
UOK146
B
UOK109 TF1 UOK120 UOK146
siCTR siTFE3 siCTR siTFE3 siCTR siTFE3 siCTR siTFE3
TFE3
VCL
C
Colony formation
Number of colonies
D
UOK109 GSEA
TF1 GSEA
UOK120 GSEA
UOK146 GSEA
Down-regulated
Up-regulated
NES
(p.val<0.05, FDR<0.25)
E
Enriched genes in Oxidative Phosphorylation Hallmark
UOK109-115genes
TF1-139genes
UOK120-123genes
UOK146-135genes
F
Complex I
Complex II
Complex III
Complex IV
Vacuolar ATPase
Others
Complexes
G
OCR (pmoles/min/10 000 cells)
Time (min)
UOK109
TF1
UOK120
UOK146
UOK121
786-O
H
Basal Respiration
Max Respiration
I
Basal OCR
Max OCR
Reserve capacity
OCR (pmol/min/10 000 cells)
siCTR
siTFE3

Figure 1

Figure 1. TFE3 fusion proteins regulate colony forming capacity and OxPhos gene expression. A. TFE3-fusion protein expression was measured by RT-qPCR 72 hours after siRNA transfection and expressed as fold change over siCTR normalized to housekeeping gene RPLP0 (n=3). Conditions were compared by paired t-test (*: p.val<0.05, ***: p.val<0.001). **B.** Immunoblot of total protein extracts after siCTR or siTFE3 treatment. TFE3 blots for UOK109/TF1 and UOK120/UOK146 lines were exposed separately for 1 second and 10 seconds respectively. VCL was used as a loading control. **C.** Cells were treated with siCTR or siTFE3 and 5000 cells seeded and cultured for 14 days, fixed and colored with crystal violet to assess colony forming ability (n=6). Conditions were compared by paired t-test (***: p.val<0.001). **D.** Gene Set Enrichment Analysis (GSEA) results comparing siCTR with siTFE3 using the Hallmark gene sets. Significantly deregulated pathways (p.val<0.05, FDR<0.25) are represented for each of the 4 lines. **E.** Venn diagram showing overlap between significantly deregulated OxPhos genes in each cell line as defined by GSEA. **F.** Heatmap showing expression of the 54-commonly down-regulated OxPhos genes as a Z-score. **G.** Measure of OCR in tRCC (UOK109, TF1, UOK120, UOK146) and ccRCC (UOK121, 786-O) cell lines (n=5). OCR values measured in tRCC and ccRCC lines were normalized by the number of cells in each well. **H.** OCR values were used to measure the basal and the maximal respiration levels and compared these levels between each tRCC and the two ccRCC lines by 1-way Anova (Dunnett's multiple comparison test, ns: non-significant – p.val>0.05, *: p.val<0.05, **: p.val<0.01, ***: p.val<0.001). **I.** Measurement of OCR in tRCC lines 72 hours after treatment with siCTR or siTFE3 (n=5). OCR values were used to measure the basal and the maximal respiration levels and reserve respiration capacity. siCTR and siTFE3 conditions were compared by paired t-test (ns: non-significant p.val>0.05, *: p.val<0.05, **: p.val<0.01). For Max OCR: p.val UOK109 = 0.0047; TF1 = 0.19; UOK120 = 0.027; U0K146 = 0.048

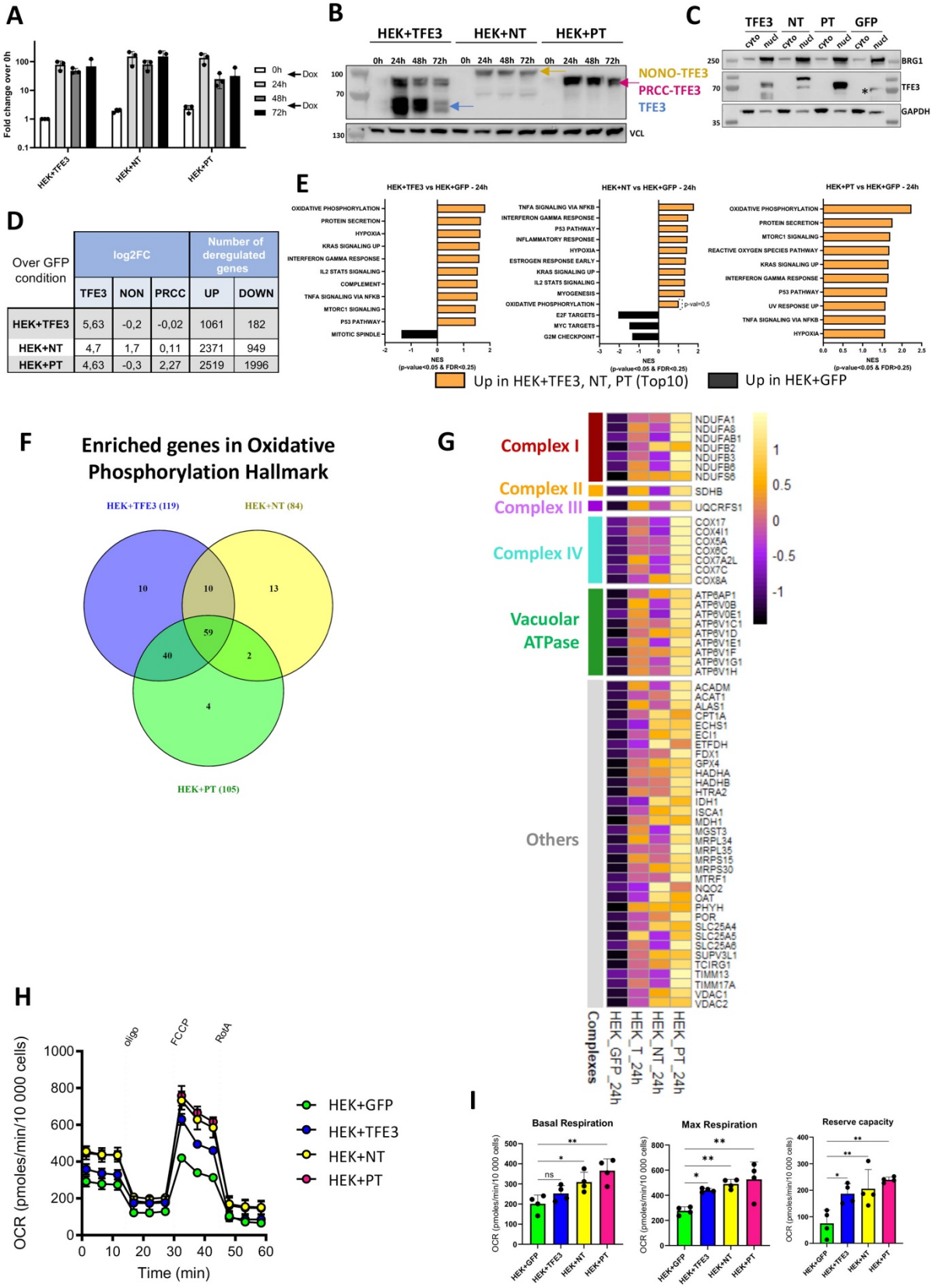
A
Fold change over 0h
0h
24h
48h
72h
Dox
HEK+TFE3
HEK+NT
HEK+PT
B
HEK+TFE3
HEK+NT
HEK+PT
0h 24h 48h 72h
NONO-TFE3
PRCC-TFE3
TFE3
VCL
C
TFE3 NT PT GFP
cyto nucl
BRG1
TFE3
GAPDH
D
Over GFP condition
log2FC
Number of deregulated genes
TFE3 NON PRCC UP DOWN
HEK+TFE3 5,63 -0,2 -0,02 1061 182
HEK+NT 4,7 1,7 0,11 2371 949
HEK+PT 4,63 -0,3 2,27 2519 1996
E
HEK+TFE3 vs HEK+GFP - 24h
HEK+NT vs HEK+GFP - 24h
HEK+PT vs HEK+GFP - 24h
OXIDATIVE PHOSPHORYLATION
PROTEIN SECRETION
HYPOXIA
KRAS SIGNALING UP
INTERFERON GAMMA RESPONSE
IL2 STAT5 SIGNALING
COMPLEMENT
TNFA SIGNALING VIA NFKB
MTORC1 SIGNALING
P53 PATHWAY
MITOTIC SPINDLE
INFLAMMATORY RESPONSE
ESTROGEN RESPONSE EARLY
MYOGENESIS
E2F TARGETS
MYC TARGETS
G2M CHECKPOINT
REACTIVE OXYGEN SPECIES PATHWAY
UV RESPONSE UP
NES
(p-value<0.05 & FDR<0.25)
(p-value<0.05 & FDR>0.25)
Up in HEK+TFE3, NT, PT (Top10)
Up in HEK+GFP
F
Enriched genes in Oxidative Phosphorylation Hallmark
HEK+TFE3 (119)
HEK+NT (84)
HEK+PT (105)
10 10 13 59 40 2 4
G
Complex I
Complex II
Complex III
Complex IV
Vacuolar ATPase
Others
NDUFA1 NDUFA8 NDUFAB1 NDUFB2 NDUFB3 NDUFB6 NDUFS6
SDHB
UQCRFS1
COX17 COX4I1 COX5A COX6C COX7A2L COX7C COX8A
ATP6AP1 ATP6V0B ATP6V0E1 ATP6V1C1 ATP6V1D ATP6V1E1 ATP6V1F ATP6V1G1 ATP6V1H
ACADM ACAT1 ALAS1 CPT1A ECHS1 ECI1 ETFDH FDX1 GPX4 HADHA HADHB HTRA2 IDH1 ISCA1 MDH1 MGST3 MRPL34 MRPL35 MRPS15 MRPS30 MTRF1 NQO2 OAT PHYH POR SLC25A4 SLC25A5 SLC25A6 SUPV3L1 TCIRG1 TIMM13 TIMM17A VDAC1 VDAC2
Complexes
HEK_GFP_24h
HEK_T_24h
HEK_NT_24h
HEK_PT_24h
H
OCR (pmoles/min/10 000 cells)
oligo
FCCP
RotA
Time (min)
HEK+GFP
HEK+TFE3
HEK+NT
HEK+PT
I
Basal Respiration
Max Respiration
Reserve capacity
ns

Figure 2

Figure 2. Enhanced OxPhos following ectopic expression of TFE3 fusions in HEK293T cells. A. Fold change of TFE3 expression compared to no-Dox treatment was measured by RT-qPCR at the indicated times after Dox addition (n=3). **B.** Immunoblots of total protein extracts after the indicated time of culture in presence of Dox. VCL was used as loading control. Blue arrow indicates native TFE3 protein, orange arrow NONO-TFE3 (NT) and pink arrow PRCC-TFE3 (PT). **C.** Western blot analysis of cytoplasmic (cyto) and nuclear (nucl) protein extracts of indicated HEK293T cell lines. BRG1 was used as positive control for the nuclear extract, GAPDH for cytoplasmic extract. * Indicates a non-specific signal in the GFP control nuclear extract. **D.** Log2FC values (over GFP) of TFE3, NONO and PRCC in each line and number of genes deregulated 24 hours after Dox addition (log2FC > ±1; adj p.val<0.05 over GFP) in each line (n=3). **E.** GSEA ontology analysis of differentially regulated genes in each cell line over GFP-line control. Significantly deregulated pathways (p.val<0.05, FDR<0.25) are represented for each of the 3 lines, restricted to the top10 pathways for HEK+PT line. **F**. Venn diagram showing overlap between significantly up-regulated OxPhos genes according to GSEA. **G.** Heatmap showing relative expression of each of the 59-commonly up-regulated OxPhos genes as a Z-score. **H.** Measurement of the OCR values following ectopic TFE3, NT or PT expression (n=4). OCR values measured in each HEK line were normalized by the number of cells in each well and used to measure the basal and the maximal respiration levels and the reserve respiration capacity. Experimental conditions were compared over the GFP-condition by 1-way Anova (Dunnett's multiple comparison test, ns: non-significant p.val>0.05, *: p.val<0.05, **: p.val<0.01).

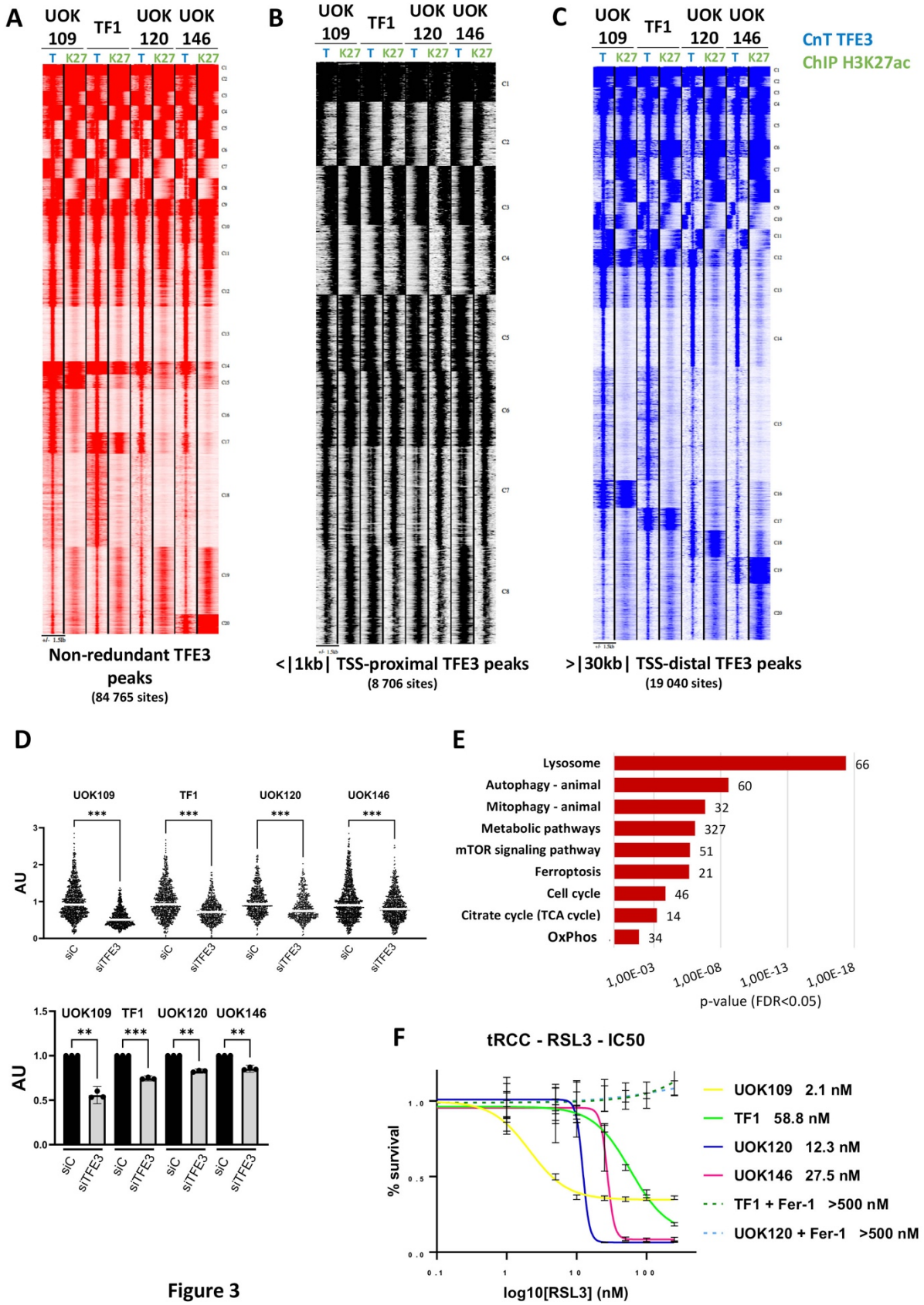
A
UOK 109
TF1
UOK 120
UOK 146
T K27 T K27 T K27 T K27
Non-redundant TFE3 peaks
(84 765 sites)
B
<|1kb| TSS-proximal TFE3 peaks
(8 706 sites)
C
>|30kb| TSS-distal TFE3 peaks
(19 040 sites)
CnT TFE3
ChIP H3K27ac
D
UOK109
TF1
UOK120
UOK146
AU
siC
siTFE3
E
Lysosome 66
Autophagy - animal 60
Mitophagy - animal 32
Metabolic pathways 327
mTOR signaling pathway 51
Ferroptosis 21
Cell cycle 46
Citrate cycle (TCA cycle) 14
OxPhos 34
1,00E-03
1,00E-08
1,00E-13
1,00E-18
p-value (FDR<0.05)
F
tRCC - RSL3 - IC50
% survival
log10[RSL3] (nM)
UOK109 2.1 nM
TF1 58.8 nM
UOK120 12.3 nM
UOK146 27.5 nM
TF1 + Fer-1 >500 nM
UOK120 + Fer-1 >500 nM

Figure 3

Figure 3. Profiling genome occupancy of TFE3 fusion proteins. A. Read density maps for TFE3 fusion protein occupancy (T) and H3K27ac (K27) at the 84 765 non-redundant sites. **B-C**. Read density maps for the non-redundant TFE3 fusion protein and H3K27ac sites at proximal promoters (<1 kb from the TSS, B) or putative distal enhancers (>30 Kb from the TSS, C). **D**. Level of EU-incorporation in each tRCC line 48 hours after siCTR or siTFE3. The upper panel shows the combined quantification of the relative EU intensity signal in the nucleus for each cell line from the 3 independent experiments normalized by the mean intensity of the control condition. Student T-test: pvalue 0.033 (*), 0,002 (**), < 0,001 (***). The lower panel shows results for the 3 independent experiments with errors bar representing 95% confidence interval. Paired Student T-test pvalue 0.033 (*), 0,002 (**), < 0,001 (***). **E.** KEGG ontology of genes associated with TFE3 fusion protein occupancy of M/E-box containing sites +/- 500 bp of the TSS. Each indicated KEGG pathway presented an FDR < 0.05 and number of genes found in each pathway were noted to the right of the bar. **F.** RSL3 IC50 values of tRCC lines in presence or absence of 1 mM ferristatin-1 (Fer-1) as indicated.

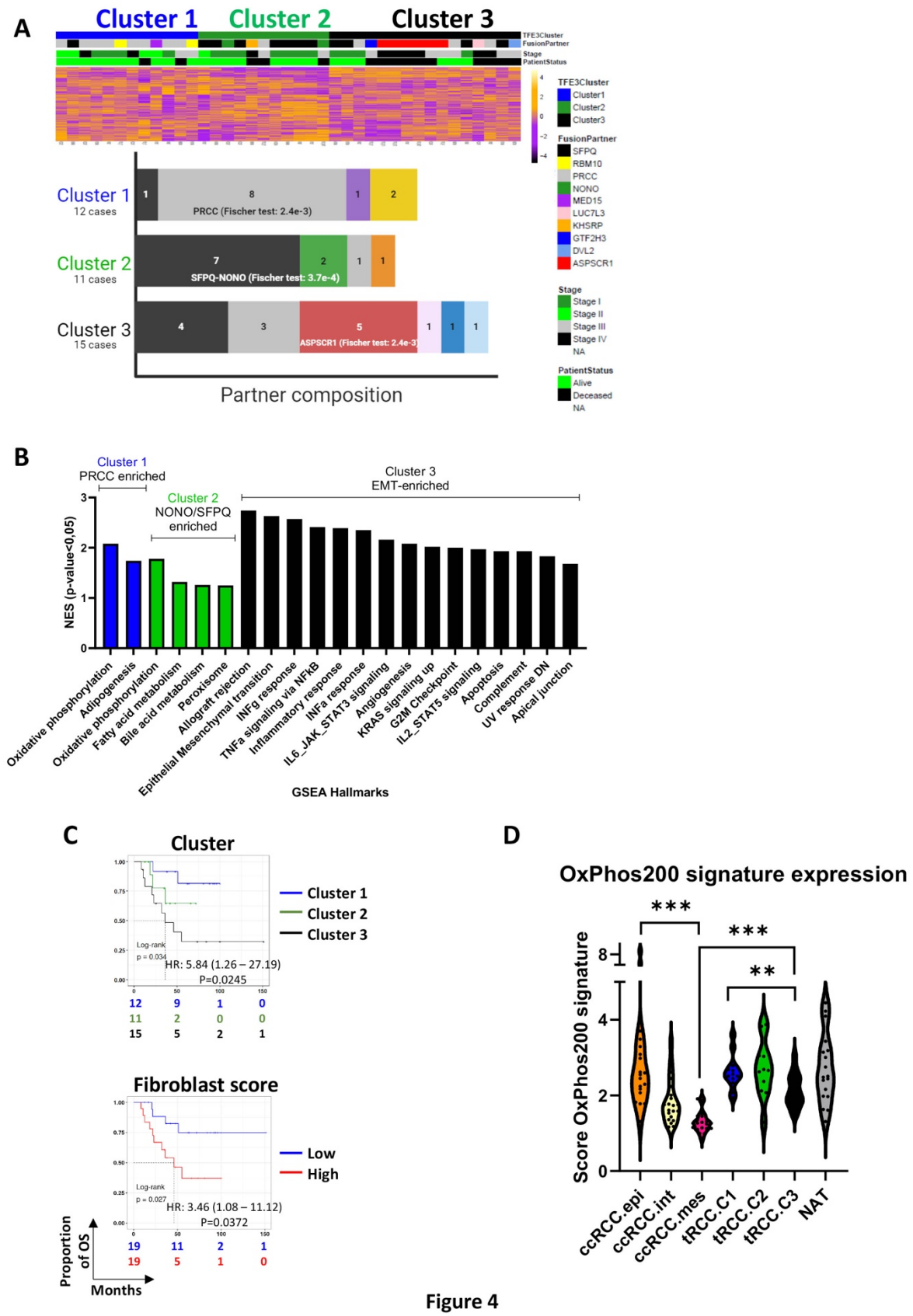

Figure 4. EMT and OxPhos in human tRCC. A. Heatmap of the unsupervised clustering of gene expression with the indicated clinical and molecular parameters, showing the distribution

of tRCC in 3 clusters. Distribution of tRCC samples according to fusion partner type within the 3 major clusters; p-values were indicated for most frequently represented partner in each cluster. **B.** GSEA ontology analyses of differentially expressed genes between the different clusters indicating the enriched terms (p.value<0.05, FDR<0.25) for each cluster (with only the top15 for Cluster 3). **C**. Kaplan-Meier curves for overall survival in tRCC patients according to classification in the three clusters or fibroblast score, calculated using MCP counter, according to the optimal cut point method with the associated log-rank p-value. Hazard ratio (HR) was calculated using univariate Cox proportional-hazards model. **D.** Expression score of the 200-signature genes of GSEA-OxPhos Hallmark in NAT, each tRCC cluster and the indicated ccRCC tumour subtypes from the TCGA KIRC collection. Overall scores were compared by Wilcoxon test (**: p.val<0.01, ***: p.val<0.001).

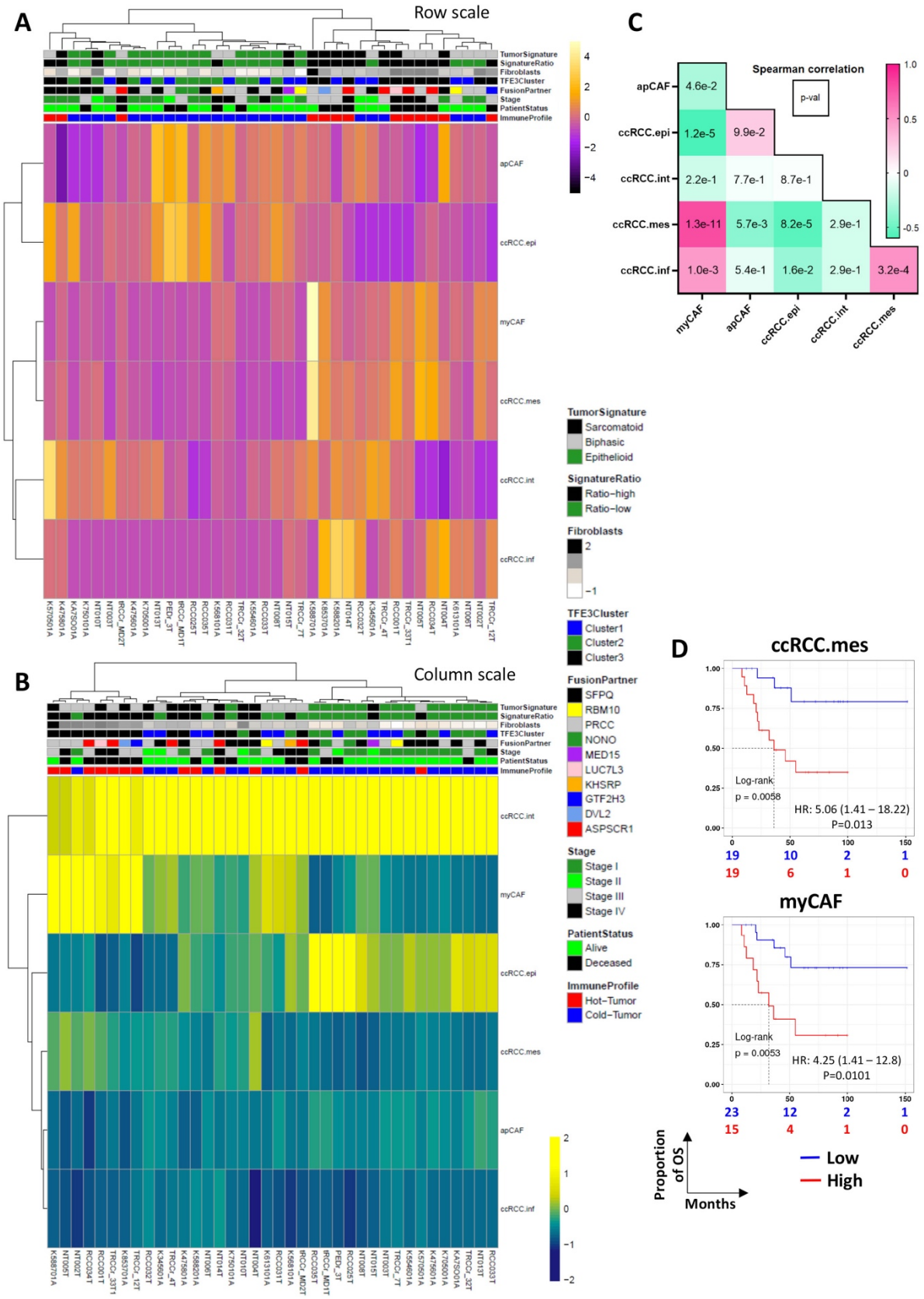
A
Row scale
B
Column scale
C
Spearman correlation
p-val
apCAF
ccRCC.epi
myCAF
ccRCC.mes
ccRCC.int
ccRCC.inf
TumorSignature
Sarcomatoid
Biphasic
Epithelioid
SignatureRatio
Ratio−high
Ratio−low
Fibroblasts
TFE3Cluster
Cluster1
Cluster2
Cluster3
FusionPartner
SFPQ
RBM10
PRCC
NONO
MED15
LUC7L3
KHSRP
GTF2H3
DVL2
ASPSCR1
Stage
Stage I
Stage II
Stage III
Stage IV
PatientStatus
Alive
Deceased
ImmuneProfile
Hot−Tumor
Cold−Tumor
D
ccRCC.mes
Log-rank
p = 0.0058
HR: 5.06 (1.41 – 18.22)
P=0.013
myCAF
Log-rank
p = 0.0053
HR: 4.25 (1.41 – 12.8)
P=0.0101
Proportion of OS
Months
Low
High

Figure 5

Figure 5. Deconvolution of tRCC tumours using ccRCC tumour cell and CAF signatures. **A-B.** Heatmaps showing deconvolution using the ccRCC tumour cell and CAF signatures inferred by CIBERSORTx and displayed as row-scaled (A) or column-scaled (B) absolute scores on bulk RNA-seq data from the tRCC tumour samples. **C.** Spearman correlation coefficient (coloured box) and associated p-value (number in box) between the indicated populations. **D.** Kaplan-Meier curves for overall survival according to the ccRCC.mes and myCAF proportions using optimal cut-off value method with the associated log-rank p-value and the HR from the univariate Cox proportional-hazards model.

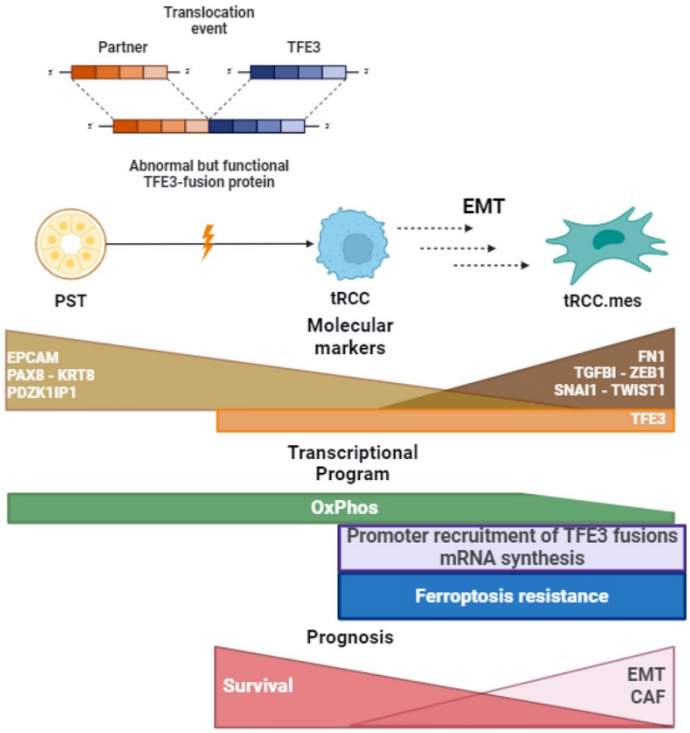

Figure 6

Figure 6. A model for TFE3-fusion protein driven tRCC. Schematic model based on the analyses in this study showing Proximal Straight Tubule (PST) cell transformation in tRCC after the translocation event involving TFE3, the EMT and its associated markers. Upon transformation, tRCC acquire ferroptosis resistance and maintain elevated OxPhos that tends to

decrease with the EMT. High nuclear accumulation of TFE3 fusions leads to their promiscuous promoter recruitment stimulating of mRNA synthesis. Finally, EMT and the presence of myCAFs correlate with poor outcome.

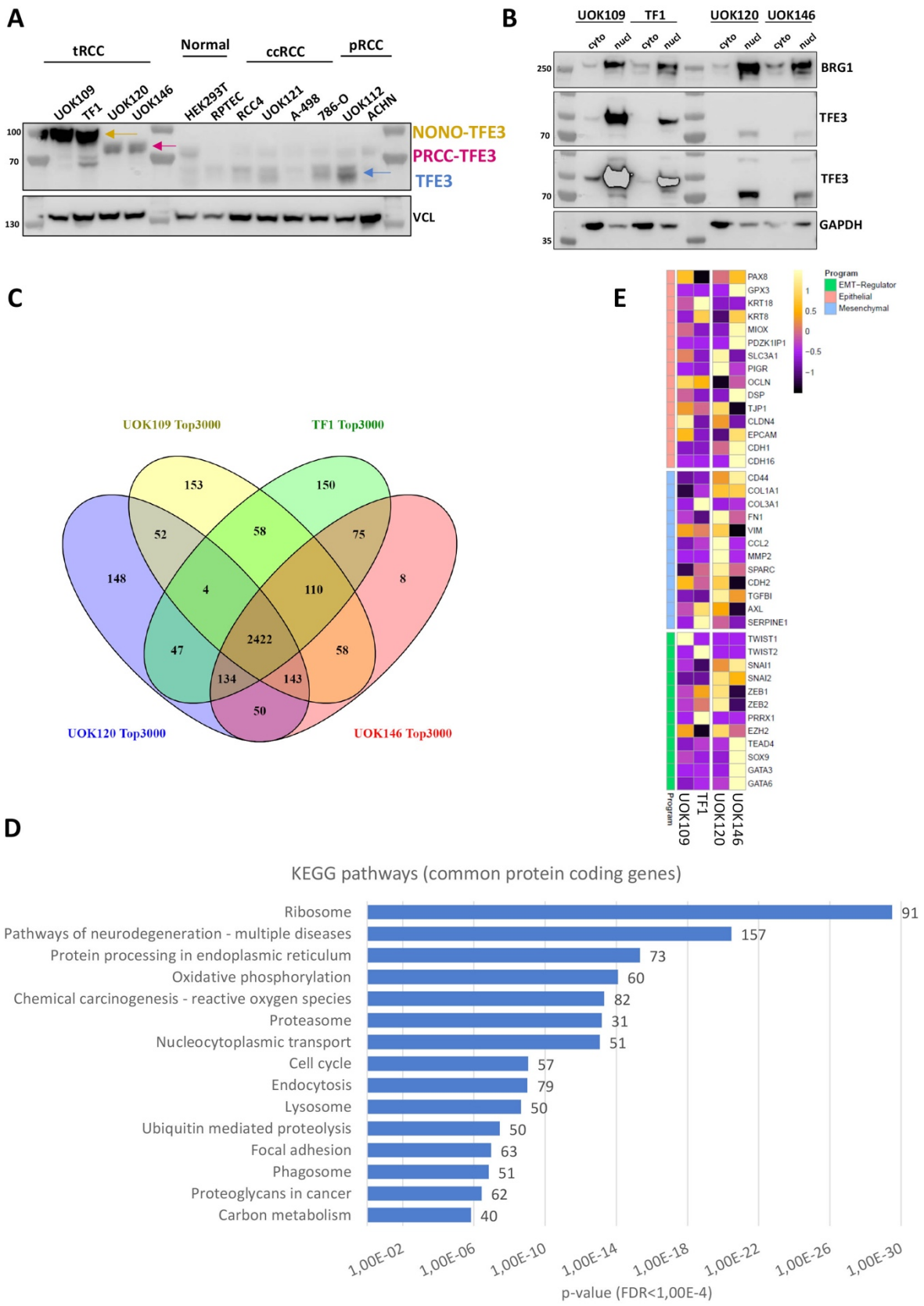

Suppl. Figure 1

Figure S1. Expression of TFE3 and its fusion proteins in cell lines. A. Western blot analysis of total protein extracts from the indicated cell lines: tRCC (UOK109, TF1, UOK120, UOK146), 'normal' kidney (HEK293T, RPTEC), ccRCC (RCC4, UOK121, A-498, 786-O) and papillary RCC (UOK112, ACHN). Vinculin (VCL) was used as loading control. Blue arrow indicates native TFE3 protein, orange arrow NONO-TFE3 and pink arrow PRCC-TFE3 fusion protein. **B.** Western blot analysis of cytoplasmic (cyto) and nuclear (nucl) fractions from the tRCC cell lines. BRG1 was used as positive control for the nuclear extract and GAPDH for cytoplasmic extract. The same blot was exposed 1 second for NONO-TFE3 and 30 seconds for PRCC-TFE3. **C.** Venn diagram indicating overlap between the 3000 most expressed protein-coding genes in each tRCC line. **D.** DAVID gene ontology analysis of the common 2422 highest expressed protein-coding genes using KEGG. Each indicated KEGG pathway presented an FDR < 10^{-4} and number of genes found in each pathway were noted to the right of the bar. **E.** Heatmap showing the expression of selected epithelial or mesenchymal marker genes in each line.

A

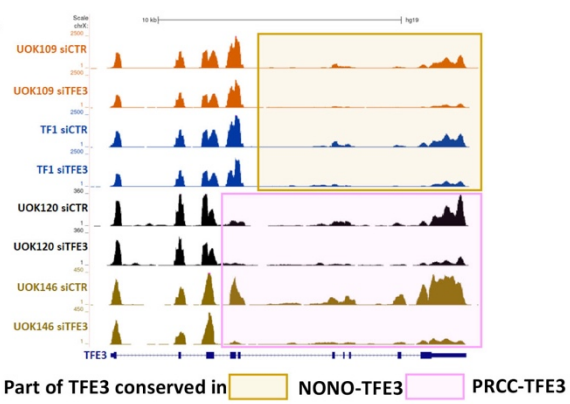

B

	Read count at fusion junction		Number of deregulated genes	
	siCTR	siTFE3	Up	Down
UOK109	72	22	186	299
TF1	119	35	598	400
UOK120	14	0	277	329
UOK146	151	11	288	356

C

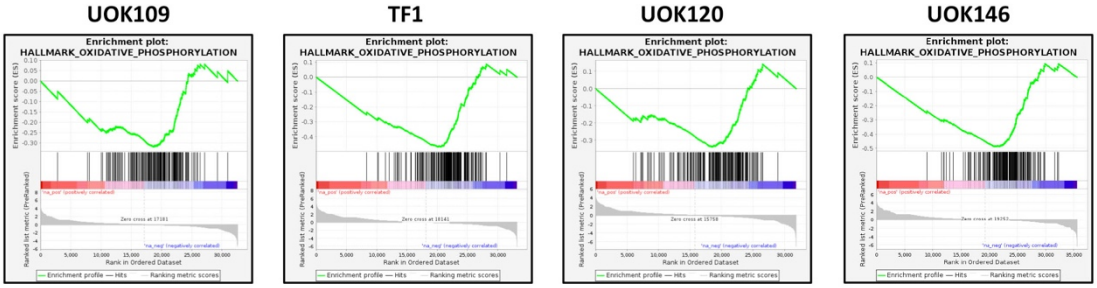

Suppl. Figure 2

Figure S2. Genes de-regulated by siTFE3 silencing. **A.** UCSC view of the RNA-seq reads at the *TFE3* gene locus. Orange box represents the TFE3 region present in NONO-TFE3 fusion, while pink box encompasses the region conserved in PRCC-TFE3 fusion. **B.** Table indicating the read count at junction between TFE3 and the fusion partners and the number of deregulated genes in siTFE3 samples compared to siCTR (log2FC > ±1; adj.p.val<0.05). **C.** Enrichment plots of the Oxidative Phosphorylation (OxPhos) pathway after GSEA analysis between siCTR and siTFE3 conditions in each line.

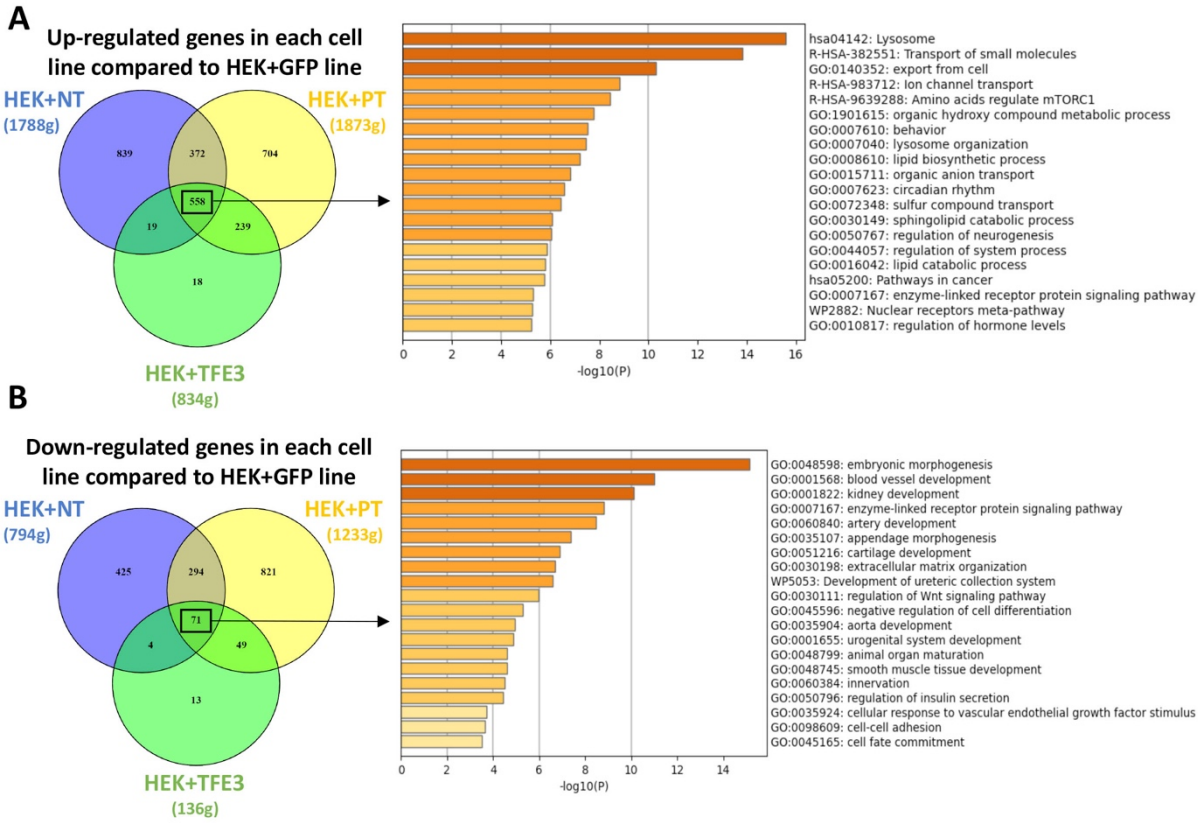

Suppl. Figure 3

Figure S3. Genes regulated by ectopically expressed TFE3 fusion proteins. A-B. Venn diagrams showing the number of deregulated genes in each line and the associated ontology analysis of the commonly regulated genes using MetaScape software. **C**. Enrichment plots of the Oxidative Phosphorylation (OxPhos) pathway according to GSEA analysis after ectopic expression of native TFE3 or NT or PT fusion proteins in HEKT cells over GFP condition.

A

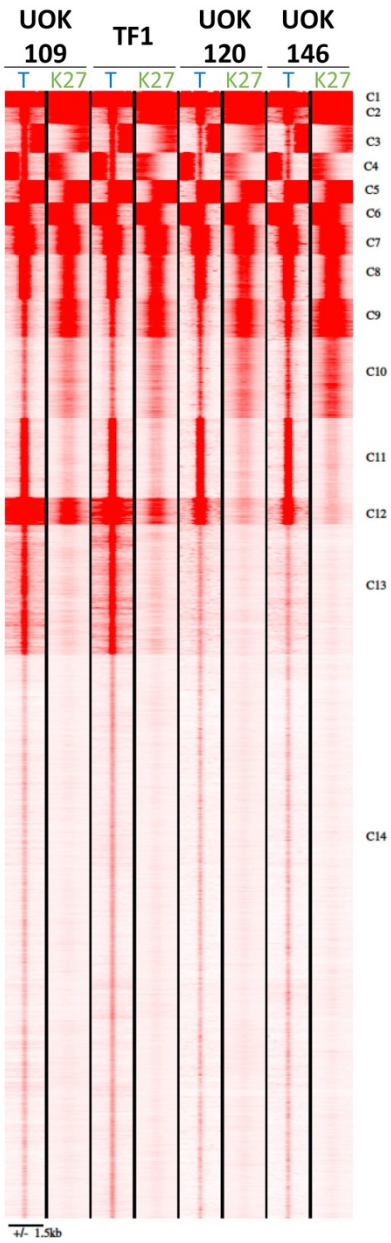

Non-redundant TFE3 peaks
(169 896 sites)

B

Cell line	Cut&Tag TFE3	ChIPseq H3K27ac	TFE3 with H3K27ac and E-box
UOK109	65901	44600	18466 (28%)
TF1	78598	56957	19919 (25%)
UOK120	33819	64545	11106 (33%)
UOK146	42760	51008	12714 (30%)

C

Cell line	Motif		e-value	Distribution
UOK109	SP2 (MA0516.3) KLF5 (MA0599.1) SP4 -MA0685.2)		3.4e-126	
	FOSL2 (MA0478.1) FOSB::JUNB (MA1135.1) FOS::JUN (MA0099.3)		2.0e-120	
	MITF (MA0620.3) TFEB (MA0692.1) TFEB_full		1.7e-53	
TF1	FOSL2 (MA0478.1) FOSL2::JUNB (MA1138.1)		4.0e-164	
	KLF12 (MA0742.2) KLF10 (MA1511.2) SP2 (MA0516.3)		8.1e-84	
	MITF (MA0620.3) USF1_DBD TFEB (MA0692.1)		3.2e-46	
UOK120	TFEB (MA0692.1) TFEB_full TFE3_DBD		3.0e-618	
UOK146	TFEB (MA0692.1) TFEB_full TFE3_DBD		8.6e-587	

D

Top1000 Peaks – RSAT analysis	UOK109		TF1		UOK120		UOK146	
Motif	Rank	e-value	Rank	e-value	Rank	e-value	Rank	e-value
MITF, USF2 motif	2	2.9e-61	6	3.4e-28	1	1.6e-66	2	6.9e-56
SP1, KLF15 motif	1	1.5e-79	1	5.6e-73	2	3.0e-54	1	3.6e-58
NFYA, NFYC motif	3	5.8e-29	3	7.6e-30	/	/	/	/

Suppl. Figure 4

Figure S4. Profiling of TFE3 fusion protein genomic occupancy. A. Read density maps for TFE3 fusion protein occupancy (T) and H3K27ac (K27) at all non-redundant sites. **B.** Total numbers of peaks with the indicated characteristics in each cell line after removal of low-occupied sites (C14 of the density map in panel A). **C.** Results of MEME-ChIP analyses of the DNA motifs at the top 1000 TFE3 bound sites in each cell line, with associated e-value and motif distribution over the peak. **D**. Results of RAST analyses of transcription factor binding motifs at the top 1000 TFE3 bound sites in each cell line showing associated rank and e-value.

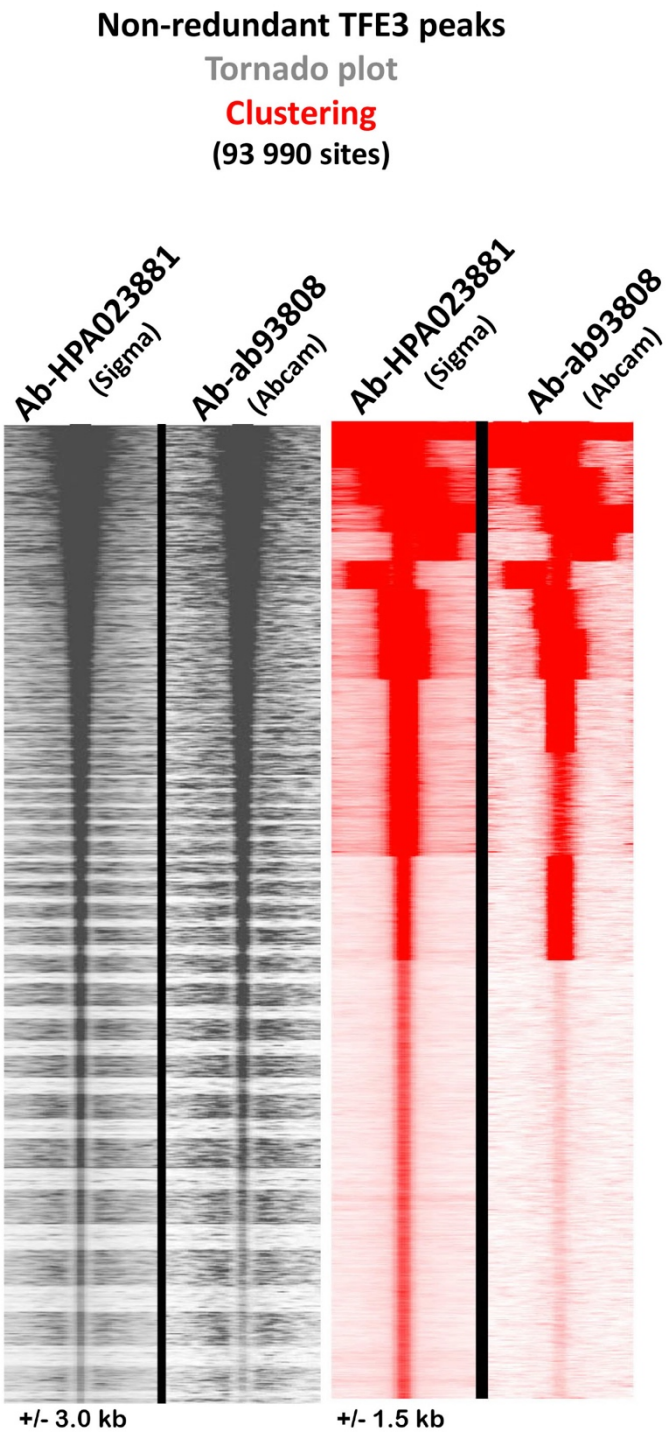

Suppl. Figure 5

Figure S5. Replicate TFE3 Cut&Tag using independent antibodies in UOK109 cells. Tornado (left panel) and read density plots (right panel) of the replicate TFE3 Cut&Tag experiments with the antibodies shown above each track.

A

HEK293T Cell line	Cut&Tag TFE3 peaks	TFE3 peaks at TSS (500nt)
+ GFP	1058	615 (58%)
+ TFE3	17250	9716 (56%)
+ NONO-TFE3	28815	14690 (51%)
+ PRCC-TFE3	20255	9707 (48%)

B

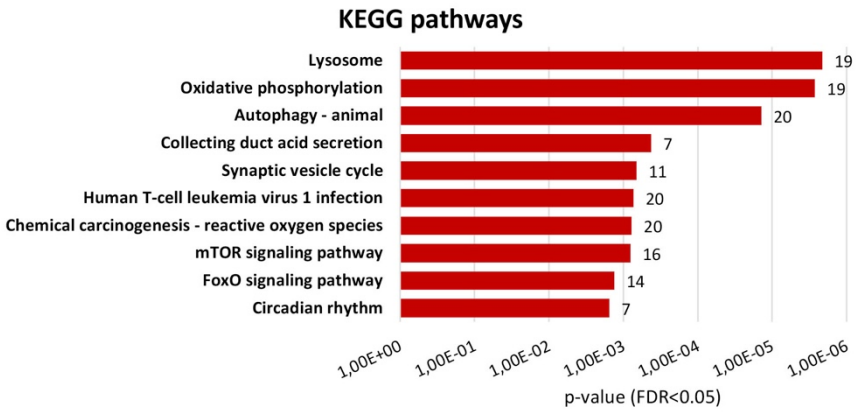

C

Cell line HEK293T +	Motif		e-value	Distribution
GFP	TFE3_DBD TFEB (MA0692.1) TFEB_full		1.0e-184	
TFE3	KLF15 (MA1513.1) KLF12 (MA0742.2) KLF10 (MA1511.2)		2.5e-203	Not centrally enriched
	TFEC (MA0871.2) USF2 (MA0526.4) Bhlhb2_primary (UP00050_1)		1.2e-54	
NONO-TFE3	KLF15 (MA1513.1) SP2 (MA0516.3) KLF12 (MA0742.2)		3.6e-428	
	NFYA (MA0060.3) NFYC (MA1644.1) NFYB (MA0502.2)		3.2e-330	
PRCC-TFE3	SP2 (MA0516.3) KLF12 (MA0742.2) KLF10 (MA1511.2)		1.6e-196	
	TFE3_DBD TFEB (MA0692.1) TFEB_full		1.1e-91	

D

Number of OxPhos genes common to the 4 tRCC lines With TFE3+H3K27ac-Ebox associated peak	
Among the 235 OxPhos-signature genes	145
Among the downregulated genes in siTFE3 (54)	33
Among the upregulated genes in HEK+ (59)	44
Among both downregulated genes in siTFE3 + upregulated genes in HEK+ (23)	19

Suppl. Figure 6

Figure S6. TFE3 binding in HEKT cells. A. Total numbers of peaks and those at the proximal promoters (500nt from the TSS) in the indicated HEKT cell line. **B.** KEGG ontology analyses of genes with binding of endogenous TFE3 in the proximal promoter in the HEK-GFP line. Each indicated KEGG pathway presented an FDR < 0.05 and number of genes found in each pathway were noted to the right of the bar. **C.** Results of MEME-ChIP analyses of the DNA motifs at the top 1000 TFE3 bound sites in each cell line, with associated e-value and motif distribution over the peak. **D.** Number of OxPhos genes in each category associated with TFE3 occupied M/E box containing a H3K27ac-marked regulatory elements common to each cell line.

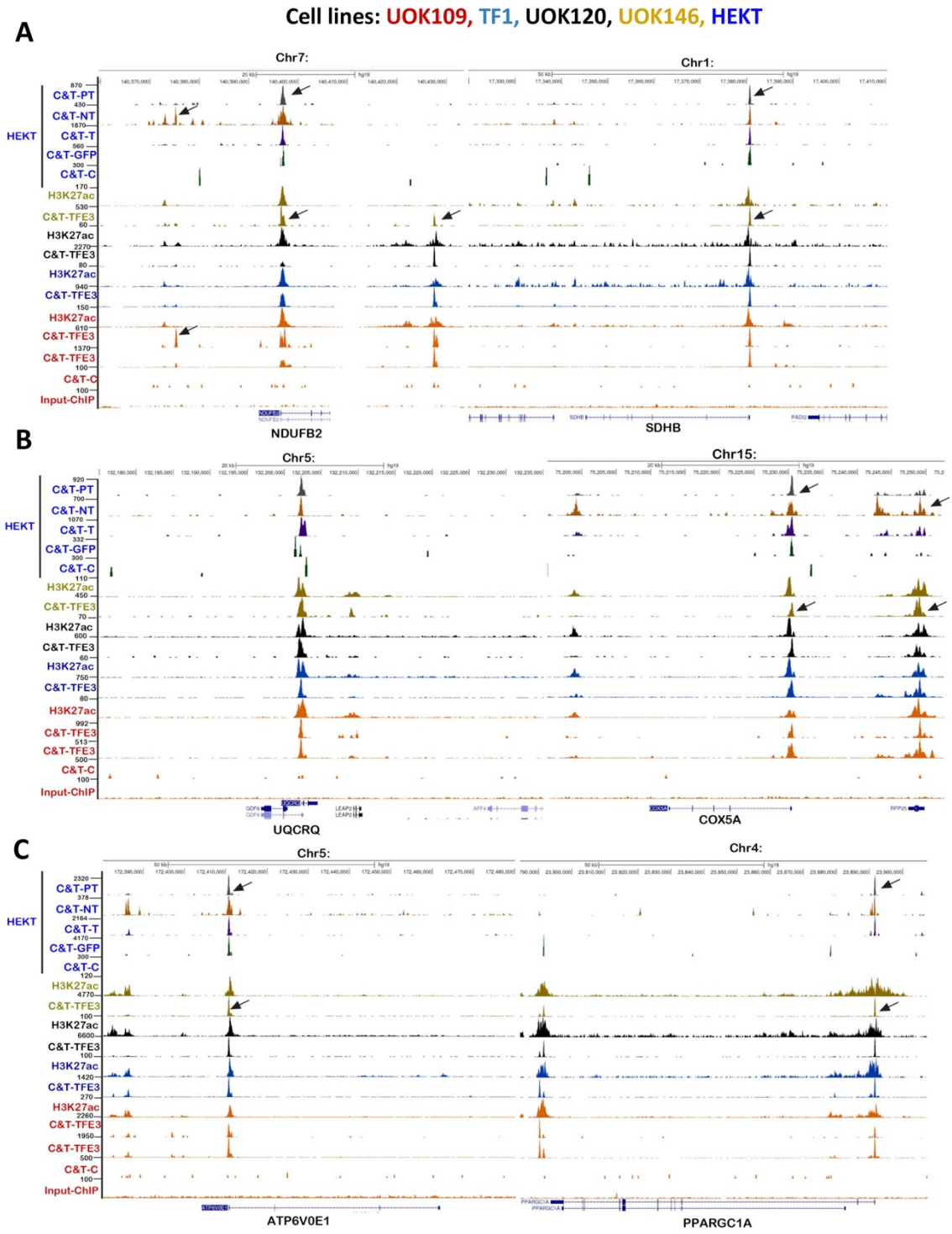

Suppl. Figure 7

Figure S7. Representative examples of TFE3 fusion protein binding at genes involved in OxPhos. A-C. UCSC genome browser views of the TFE3 C&T, and H3K27ac ChIP-seq in

each cell line, as indicated by the colour code, at the indicated loci: *NDUFB2* complex I (A, left panel); *SDHB* complex II (A, right panel); *UQCRQ* complex III (B, left panel), *COX5A* complex IV (B, right panel), the *ATPV6V0E1* (C, left panel) and *PPARGC1A* (C, right panel) gene loci. Arrows indicate TFE3 binding to H3K27ac-maked sites comprising an M-box motif.

A

Cell lines: UOK109, TF1, UOK120, UOK146, HEKT

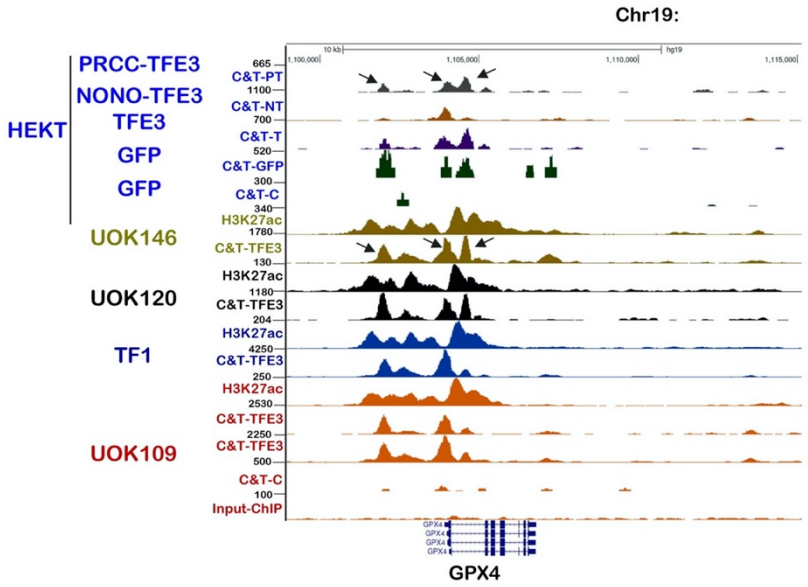

B

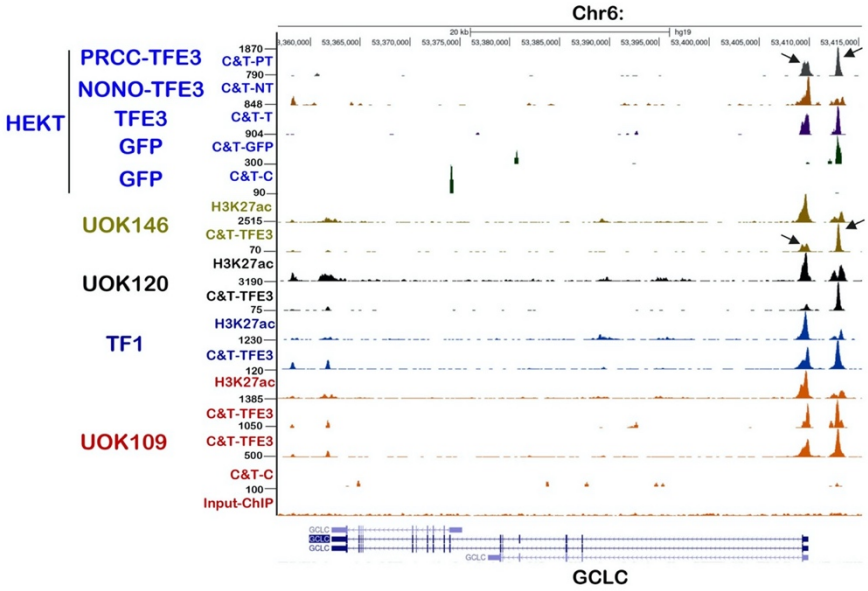

C

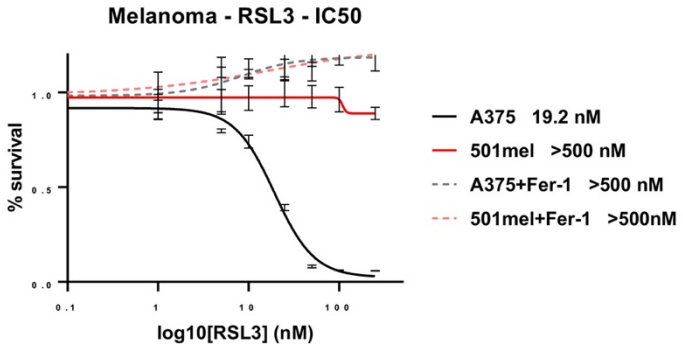

Suppl. Figure 8

Figure S8. TFE3 fusion regulation of ferroptosis. A-B. UCSC genome browser views of the TFE3 C&T, ATAC-seq and H3K27ac ChIP-seq in each tRCC and HEKT cell line, as indicated by the colour code, at the GPX4 (A) and GCLC (B) loci. **C**. RSL3 IC50 values of control melanoma lines in presence or absence of 1 mM ferristatin-1 (Fer-1) as indicated.

A

Clinicopathologic characteristics	Total (n=38)	M stage, n (%)	
Age, median (range)	33.5 (3-65)	M0	29 (76.31%)
Gender, n (%)		M1	6 (15.79%)
Male	13 (34.21%)	M2	1 (2.63%)
Female	25 (65.79%)	Mx	2 (5.26%)
T stage, n (%)		**Stage, n (%)**	
≤T2	23 (60.53%)	I-II	20 (52.63%)
≥T3	15 (39.47%)	III-IV	18 (47.37%)
N stage, n (%)		**Alive status, n (%)**	
N0	24 (63.16%)	Alive	24 (63.16%)
N1	6 (15.79%)	Dead	14 (36.84%)
N2	4 (10.53%)	**OS, median (range) (months)**	47 (8.33-231.17)
Nx	4 (10.52%)		

B

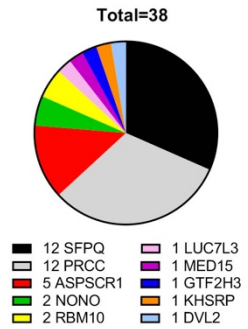

C

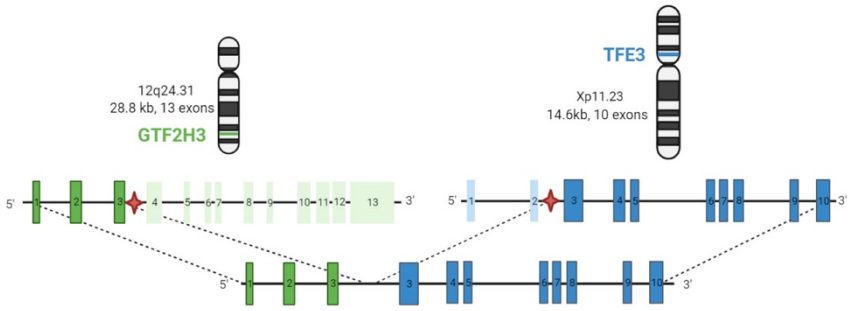

Fusion transcript GTF2H3(e1-3)-TFE3(e3-10)

D

Gene ontology on protein coding genes upregulated in Tumor samples vs NAT (2856g)

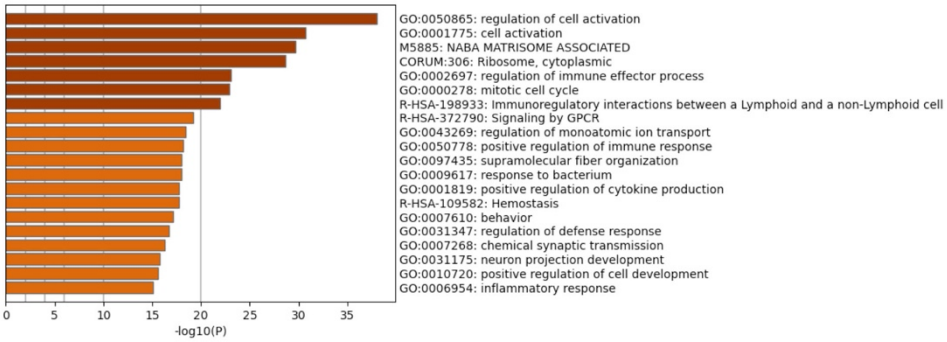

E

Gene ontology on protein coding genes upregulated in NAT vs Tumor samples (2146g)

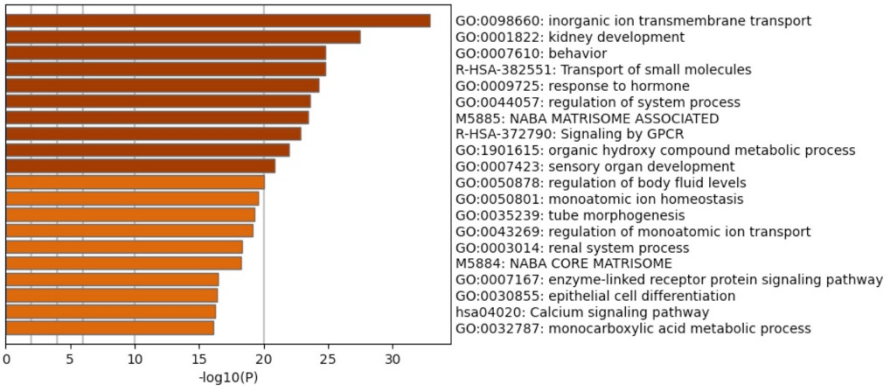

Suppl. Figure 9

Figure S9. Clinical characteristics of the tRCC cohort. A. Table presenting the clinical and pathology characteristics of the tRCC patient tumor cohort. **B**. Pie chart showing the contribution of the indicated fusion partners to the cohort. **C.** Schematic representation of a novel *TFE3* fusion with *GTF2H3* encoding the p34 subunit of general transcription factor TFIIH. **D-E**. Ontology of genes up- (D) or down- (E) regulated in tRCC tumours compared with NAT.

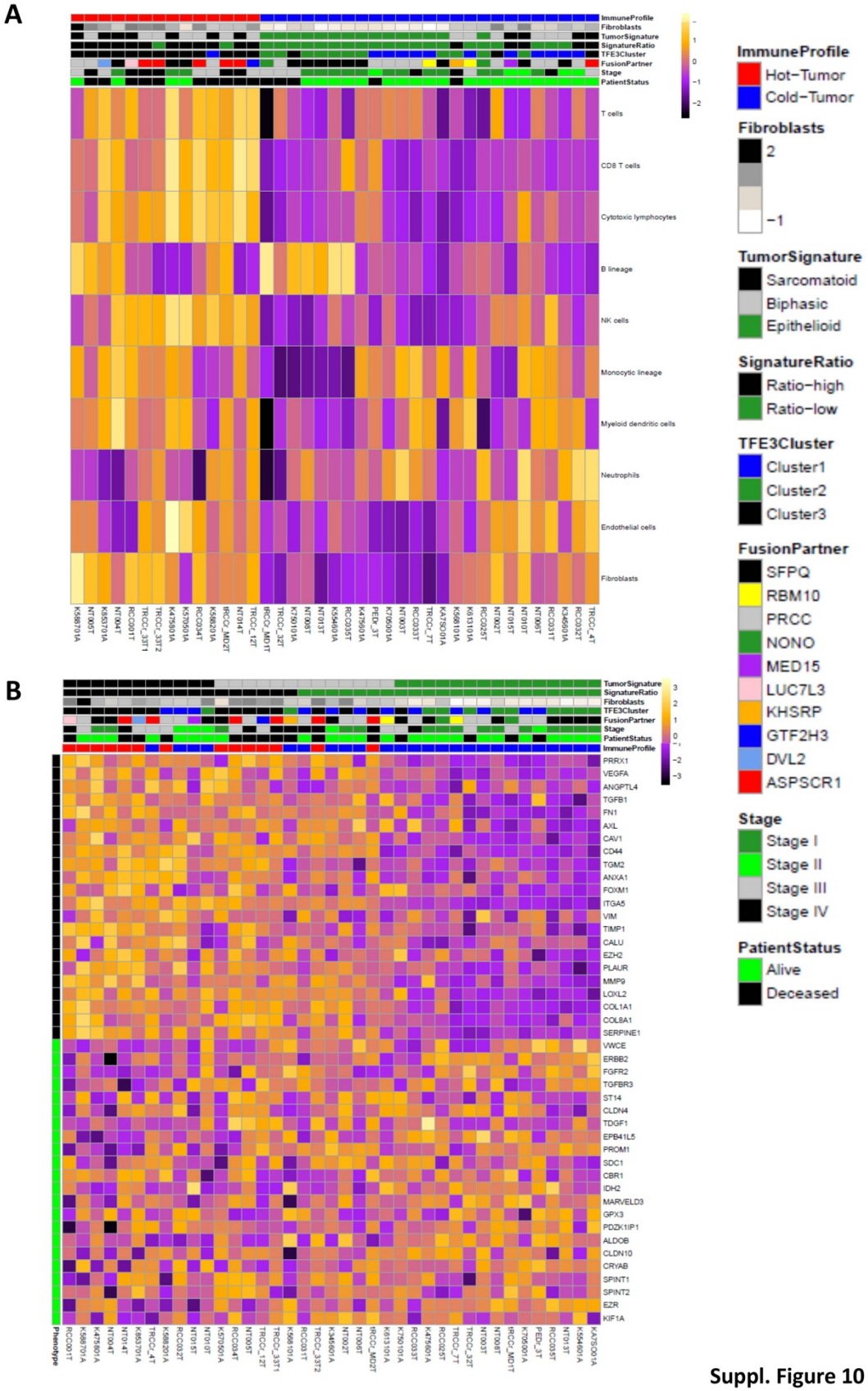

Suppl. Figure 10

Figure S10. Immune infiltration and EMT in tRCC. A. MCP counter analyses of the tRCC cohort. **B.** Heatmap of the differential expression of a collection of epithelial and EMT related makers in the tRCC cohort displayed as a Z score.

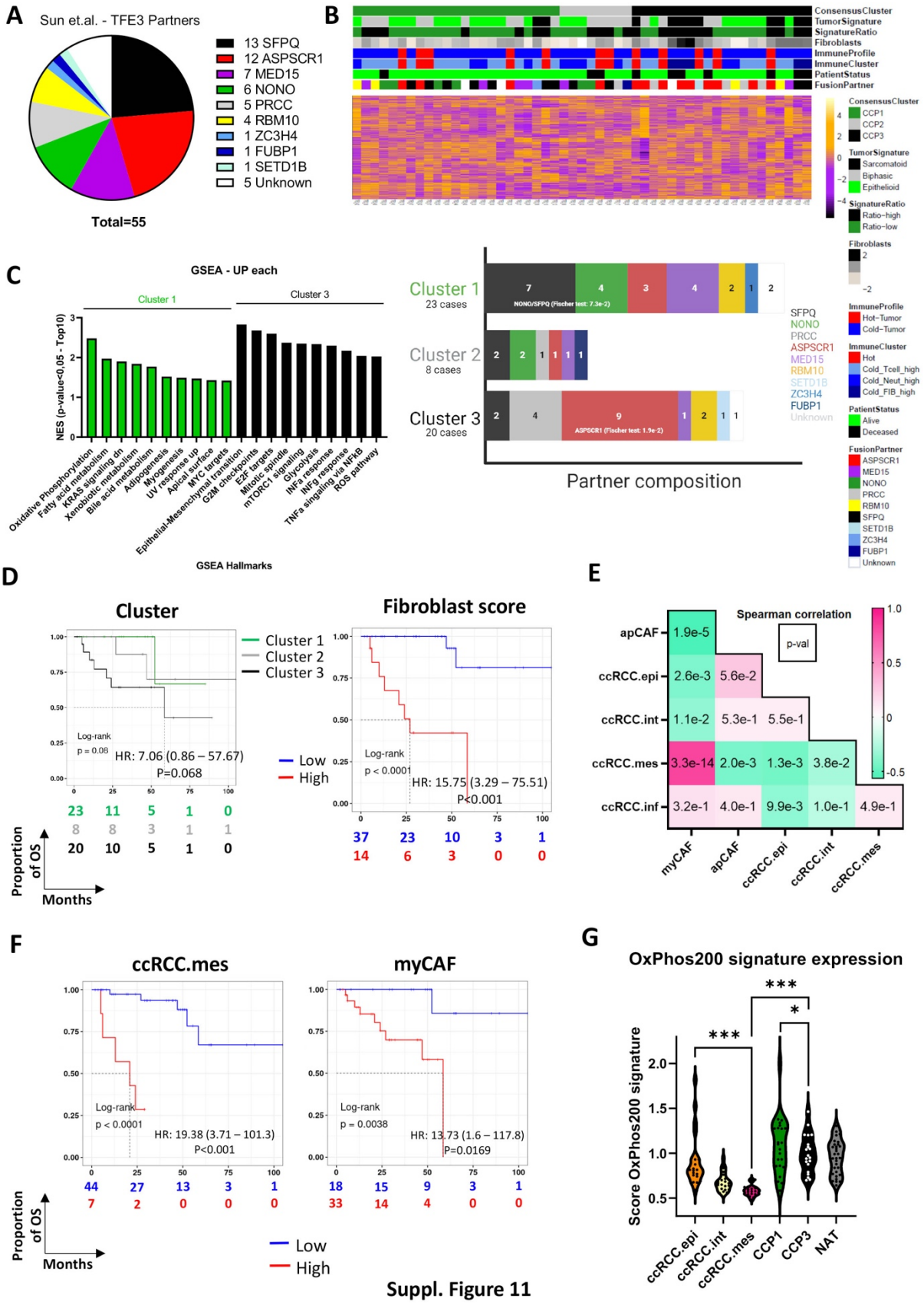

Suppl. Figure 11

Figure S11. Clinical and molecular characteristics of an independent tRCC cohort. A. Pie chart showing the contribution of the indicated fusion partners to the cohort. **B.** Heatmap of the unsupervised clustering with the indicated clinical and molecular parameters showing the division of samples in 3 clusters (upper panel). Distribution of samples by fusion partner within the 3 major clusters (lower panel). **C.** GSEA analyses of genes differentially expressed between clusters 1 and 3 indicating the Top10 enriched terms (p-value<0.05, FDR<0.05). **D**. Kaplan-Meier curves for overall survival in patients according to the cluster or the fibroblast score, calculated from MCP-counter, using the optimal cut point method with the associated log-rank p-value and Hazard ratio (HR) from the univariate Cox proportional-hazard model. **E.** Spearman correlation coefficient (coloured box) and associated p-value (number in box) between the indicated populations after deconvolution using the ccRCC tumour cell and CAF signatures inferred by CIBERSORTx on bulk RNA-seq data from the tRCC tumour samples. **F.** Kaplan-Meier curves for overall survival in patients according to ccRCC.mes or myCAF scores using the optimal cut point method with the associated log-rank p-value and Hazard ratio (HR) from the univariate Cox proportional-hazard model. **G**. Expression score of the OxPhos genes in NAT, each tRCC cluster and the indicated ccRCC tumour types from the TCGA.KIRC collection. Overall scores were compared by Wilcoxon test (*: p.val<0.05, **: p.val<0.01, ***: p.val<0.001).

Supplemental Dataset 1. Genes up and down regulated by siTFE3 compared to siCTR in each tRCC cell line. On each spreadsheet are indicated Gene name, Ensemble gene ID, Description, normalized reads in each condition, Log2 fold change and adjusted p-value. Note for up-regulated genes log2 fold change > + 1, and adjusted p-value <0.05, but for down-regulated genes log2 fold change <- 0,5, and adjusted p-value <0.05.

Supplemental Dataset 2. OxPhos Genes. Page 1. Legend, **Page 2**. List of OxPhos genes from the GSEA signature, **Page 3.** non-redundant list of OxPhos genes from the GSEA and KEGG signatures signature.

Supplemental Dataset 3. Genes up and down regulated by ectopic TFE3 and fusion protein expression in HEKT cells. On each spreadsheet are indicated. Ensemble gene ID, Gene name, Description, gene biotype (only coding genes are listed) GO, normalized reads in each condition, Log2 fold change and adjusted p-value.

Supplemental Dataset 4. Page 1. List of E/M-box containing peaks in open chromatin comment to all 4 tRCC cell lines. Indicated are peak ID, Peak coordinates, Chromosomal locations of peaks, locations relative to gene, distance to TSS, nearest Ensemble ID of nearest promoter, gene name and description. **Page 2.** Core program of protein coding genes with a TFE3 peak +/- 500 nt from the TSS. **Page 3.** KEGG ontology analyses of the core program protein coding genes.